RESEARCH ARTICLE

Key Points:
- We study Saturn's postequinox magnetosphere-ionosphere currents (2012/2013), comparing with previous analyses of preequinox currents (2008)
- Subcorotation currents have similar ~6-MA totals north and south, but a central polar current "hole" occurs in both winter hemispheres
- PPO currents are dual modulated by both systems in both hemispheres in 2012/2013 but only in the north in 2008

Correspondence to:
T. J. Bradley,
tb252@le.ac.uk

Field-Aligned Currents in Saturn's Nightside Magnetosphere: Subcorotation and Planetary Period Oscillation Components During Northern Spring

T. J. Bradley[1] (ID), S. W. H. Cowley[1] (ID), G. Provan[1] (ID), G. J. Hunt[2] (ID), E. J. Bunce[1] (ID), S. J. Wharton[1] (ID), I. I. Alexeev[3] (ID), E. S. Belenkaya[3] (ID), V. V. Kalegaev[3] (ID), and M. K. Dougherty[2] (ID)

[1]Department of Physics and Astronomy, University of Leicester, Leicester, UK, [2]Blackett Laboratory, Imperial College London, London, UK, [3]Federal State Budget Educational Institution of Higher Education M. V. Lomonosov Moscow State University, Skobeltsyn Institute of Nuclear Physics, Moscow, Russia

Abstract We newly analyze Cassini magnetic field data from the 2012/2013 Saturn northern spring interval of highly inclined orbits and compare them with similar data from late southern summer in 2008, thus providing unique information on the seasonality of the currents that couple momentum between Saturn's ionosphere and magnetosphere. Inferred meridional ionospheric currents in both cases consist of a steady component related to plasma subcorotation, together with the rotating current systems of the northern and southern planetary period oscillations (PPOs). Subcorotation currents during the two intervals show opposite north-south polar region asymmetries, with strong equatorward currents flowing in the summer hemispheres but only weak currents flowing to within a few degrees of the open-closed boundary (OCB) in the winter hemispheres, inferred due to weak polar ionospheric conductivities. Currents peak at ~ 1 MA rad^{-1} in both hemispheres just equatorward of the open-closed boundary, associated with total downward polar currents ~6 MA, then fall across the narrow auroral upward current region to small values at subauroral latitudes. PPO-related currents have a similar form in both summer and winter with principal upward and downward field-aligned currents peaking at ~ 1.25 MA rad^{-1} being essentially collocated with the auroral upward current and approximately equal in strength. Though northern and southern PPO currents were approximately equal during both intervals, the currents in both hemispheres were dual modulated by both systems during 2012/2013, with approximately half the main current closing in the opposite ionosphere and half cross field in the magnetosphere, while only the northern hemisphere currents were similarly dual modulated in 2008.

1. Introduction

The large-scale electric currents that flow between the ionosphere and magnetosphere in planetary plasma systems are a fundamental feature associated with the transfer of momentum between these regions (e.g., Cowley, 2000; Hunt et al., 2018). At Saturn, as the subject of the present paper, two current systems have been identified via their associated perturbation magnetic fields and have been extensively studied using data from the Cassini spacecraft (Bunce et al., 2008; Hunt et al., 2014, 2015, 2016; Southwood & Kivelson, 2009; Talboys et al., 2011; Talboys, Arridge, Bunce, Coates, Cowley, & Dougherty, 2009; Talboys, Arridge, Bunce, Coates, Cowley, Dougherty, & Khurana, 2009). The first of these is the quasi-steady currents associated with subcorotation of the magnetospheric plasma relative to the neutral upper atmospheric flow, resulting from charged particle pickup and outward radial transport from the water gas source at the moon Enceladus on closed field lines, together with effects associated with the solar wind interaction on open field lines (e.g., Hill, 1979; Isbell et al., 1984; Cowley & Bunce, 2003; Cowley, Bunce, & Prangé, 2004; Pontius & Hill, 2009; Bagenal & Delamere, 2011). The second is the current systems associated with the planetary period oscillation (PPO) phenomenon, related to twin-vortex flows in the northern and southern polar ionospheres, which rotate around the planetary axis with close but separate periods near to ~10.7 hr, whose oscillatory effects are ubiquitous throughout Saturn's magnetosphere (Andrews, Cowley, et al., 2010; Carbary & Mitchell, 2013; Espinosa & Dougherty, 2000; Gurnett et al., 2009; Hunt et al., 2014; Jia & Kivelson, 2012; Jia et al., 2012; Southwood & Cowley, 2014). In principle, a third current system may also be present associated with solar wind driving of Earth-like magnetospheric flow, which is fixed in local time (LT) and oppositely directed at dawn and dusk (Cowley, Bunce, & O'Rourke, 2004; Jackman & Cowley, 2006; Southwood & Kivelson, 2009). However, no such effect has been demonstrated in Cassini field data to date (Hunt et al., 2016).
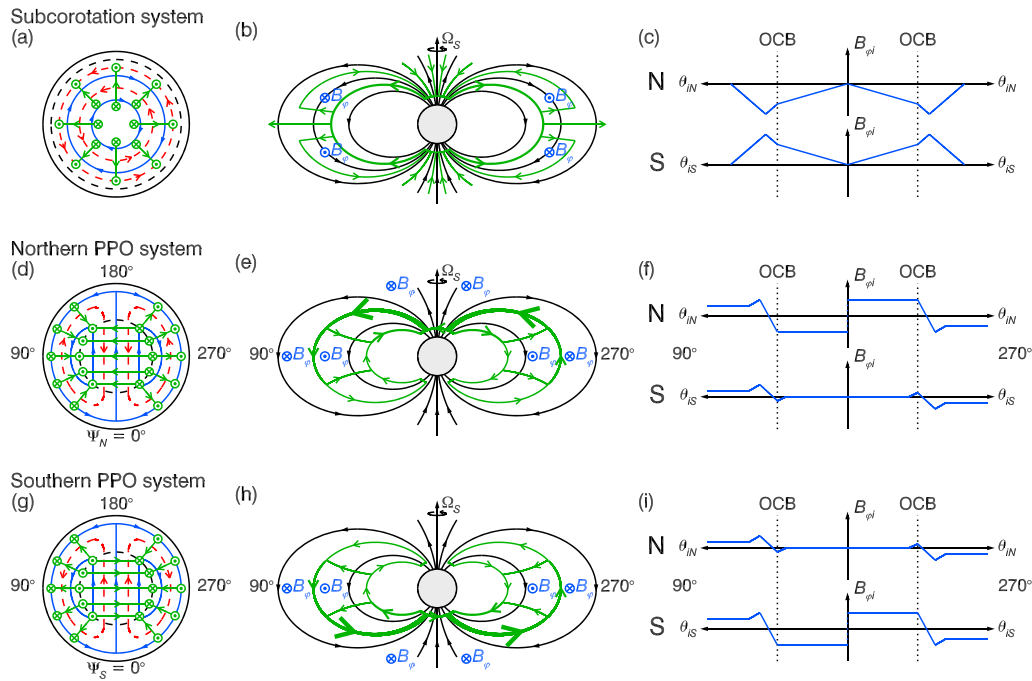
Figure 1. Sketches showing the Saturn magnetosphere-ionosphere current systems and related magnetic field perturbations associated with plasma subcorotation (Figures 1a–1c) and northern and southern PPO current systems (Figures 1d–1f and 1g–1i, respectively). Green arrowed lines and symbols show electric currents, while blue arrowed lines and symbols show associated magnetic field perturbations. Circled dots and crosses indicate vectors pointing out of and into the plane of the diagram, respectively. Figures 1a, 1d, and 1g show Saturn's polar regions viewed from above the north pole (i.e., looking along the magnetic/spin axis), where Figures 1a and 1d show the north polar region and Figure 1g the south polar region viewed through the planet from the north. Red arrowed dashed lines show the sense of the atmospheric/ionospheric flow associated with each current system. Figures 1d and 1g also illustrate the northern and southern PPO azimuthal phase systems employed, with $\Psi_{N,S} = 0°$ at the bottom of each sketch, increasing clockwise around the planet as viewed from the north. Figures 1b, 1e, and 1h show the current systems and field perturbations in the $\Psi_{N,S} = 90° − 270°$ meridian plane, where the black arrowed lines indicate Saturn's background magnetic field. Figures 1c, 1f, and 1i show sketches of the azimuthal perturbation field ($B_{\varphi i}$) above the northern (N, upper) and southern (S, lower) ionospheres for each current system, where the central vertical arrowed lines mark the poles, with colatitude away from the pole increasing on both sides, θ_{iN} in the north and θ_{iS} in the south. Vertical dotted lines indicate the location of the open-closed boundary (OCB).

1.1. Subcorotation and PPO Current Systems

The principal features of the subcorotation and PPO-related current systems at Saturn discerned from the recent studies cited above are sketched in Figure 1, adapted from Hunt et al. (2015), where Figures 1a–1c show the subcorotation current system, while Figures 1d–1f and 1g–1i show the northern and southern PPO-related currents, respectively. In this figure the currents are indicated by green arrowed lines and symbols and the magnetic perturbation fields by blue arrowed lines and symbols, where circled dots and crosses indicate vectors pointing out of or into the plane of the figure, respectively. Figures 1a, 1d, and 1g show the ionospheric currents in a view looking down from the north, "through" the planet in the case of the southern PPO system in Figure 1g. Arrowed red dashed lines show the atmospheric/ionospheric flows associated with each system, assuming that the PPOs are driven outward from the planetary atmosphere in Figures 1d and 1g. Figures 1b, 1e, and 1h show the currents and perturbation fields in a magnetic meridian plane (the principal meridian for the PPO currents as discussed further below), where the black arrowed lines show the background magnetic field, approximately symmetric about Saturn's rotation axis (Burton et al., 2010). For future reference, Figures 1c, 1f, and 1i show sketches in the same meridian planes of the azimuthal field perturbations just above the ionosphere, $B_{\varphi i}$, for both the northern (N) and southern (S) hemispheres. The central vertical arrowed lines mark the position of the poles, with colatitude from the poles increasing on either side, θ_{iN} in the north and θ_{iS} in the south. Vertical dotted lines indicate the location of the open-closed field line boundary (OCB) (Gurnett et al., 2010; Jinks et al., 2014).

1.1.1. Subcorotation Current System

Given the polarity of Saturn's internal field, opposite to Earth, the subcorotation current system in Figures 1a–1c consists of a distributed current flowing downward over the subcorotating polar regions, closed by a ring

of upward current flowing at lower latitudes in each hemisphere where the plasma angular velocity increases toward that of the planet, Ω_S (Cowley et al., 2008; Cowley & Bunce, 2003; Cowley, Bunce, & O'Rourke, 2004; Hill, 1979). Note that throughout this paper "upward" and "downward" are with respect to the planet and its upper atmosphere/ionosphere, that is, approximately radially outward and inward, respectively. The torque associated with the $j \times B$ force of the related equatorward directed ionospheric Pedersen current (Figure 1a) balances the frictional torque due to ion-neutral collisions in the ionosphere, with this torque being transferred to the equatorial plasma via the closure currents directed radially outward in the magnetosphere. The associated magnetic perturbations (Figure 1b) result in magnetospheric field lines being bent out of meridian planes into a "lagging" configuration, with negative azimuthal fields in the northern hemisphere and positive azimuthal fields in the southern hemisphere. Dynamics resulting in supercorotation of the magnetospheric plasma would correspondingly produce a "leading" configuration with reversed azimuthal fields, currents, and angular momentum transfer. Given subcorotation, the azimuthal field just above the ionosphere (Figure 1c) increases monotonically from zero at each pole due to the increase in atmospheric velocity with distance from the rotation axis, then more rapidly across the OCB associated with an increase in ionospheric conductivity due to hot plasma precipitation on closed field lines, and then returns near to zero across the ring of upward directed current at lower latitudes (e.g., Hunt et al., 2014, 2015). In the equatorial plane the upward field-aligned current region extends inward to radial distances of ~10 R_S (where R_S is Saturn's 1-bar equatorial radius equal to 60,268 km). In Figures 1b and 1c these perturbations are shown for simplicity as being of equal magnitude in the northern and southern hemispheres, though as we will see in this paper, significant differences occur related to Saturn's seasons.

1.1.2. PPO Current Systems

By comparison, the principal currents of the two PPO systems flow into the ionosphere on one side of the planet and out on the other side (Figures 1d, 1e, 1g, and 1h), closing partly across the corresponding polar ionosphere, partly through the near-equatorial magnetosphere, and partly via the opposite ionosphere, where the cross-field currents are again associated with a $j \times B$ force on the plasma (Andrews, Cowley, et al., 2010; Southwood & Cowley, 2014). These systems generate a quasi-uniform perturbation field in the near-equatorial region interior to the field-aligned currents, directed outward in both Figures 1e and 1h, which weakens in the inner regions of the magnetosphere across the interior closure currents. This perturbation field closes principally over the corresponding pole, north for the northern system in Figure 1e and south for southern system in Figure 1h, extending also into the equatorial region, as shown by the fields directed into the plane in these figures. In these regions the perturbation takes the form of a quasi-dipolar field with the effective dipole being transverse to the spin axis and directed out of the diagrams in Figures 1e and 1h. However, these closure fields have been found not to extend with measureable amplitude over the "opposite" poles (Andrews et al., 2012; Hunt et al., 2015). These features are reflected in the ionospheric perturbation fields sketched in Figures 1f and 1i, where the apparent discontinuity in field value at the pole is due only to the switch in sense of the azimuthal unit vector across this axis. We note that in the equatorial region the transition of the perturbation field from quasi-uniform to quasi-dipolar, associated with a reversal in sense of the azimuthal field component, takes place at radial distances of ~15–20 R_S, while the main PPO currents extend inward to ~10 R_S (similar to the subcorotation upward current), and the closure currents to inside of ~5 R_S (Andrews, Coates, et al., 2010; Hunt et al., 2014, 2015). For comparison, a typical stand-off distance of the subsolar magnetopause is ~25 R_S (e.g., Kanani et al., 2010; Pilkington et al., 2015).

Azimuthal position with respect to the PPO systems is defined through the phase functions Ψ_N for the northern system and Ψ_S for the southern system, as shown in the polar views in Figures 1d and 1g. These are defined for both systems such that the equatorial quasi-uniform perturbation field points radially outward at $\Psi_{N,S} = 0°$. Figures 1e and 1h then show cuts in the $\Psi_{N,S} = 90° - 270°$ meridian plane, as marked in those figures. The radial fields thus vary throughout the domain as ~ $\cos \Psi_{N,S}$, while the azimuthal fields vary as ~ $\sin \Psi_{N,S}$ in the quasi-uniform field region, in lagging quadrature with the radial field, and as ~ $- \sin \Psi_{N,S}$ in the quasi-dipolar field region, in leading quadrature with the radial field. Colatitudinal perturbation fields are also present joining the near-equatorial and polar perturbation field regions, which vary as ~ $- \cos \Psi_N$ for the northern system, in antiphase with the radial field, and ~ $\cos \Psi_S$ for the southern system, in phase with the radial field. These two systems then rotate about the planetary axis with (in general) separate periods close to that of the planetary rotation period, such that $\Psi_{N,S}$ increase monotonically with time at a fixed position. As discussed further in section 1.3, the periods of the two systems vary by ~±1% about ~10.7 hr over

Saturn's seasons, compared with a value of ~10.57 hr for Saturn's deep rotation period estimated by Read et al. (2009) from atmospheric dynamics considerations.

1.2. Cassini Measurements of Field-Aligned Current Signatures

As is clear from Figure 1, field-aligned current signatures can be determined from latitude profiles of the associated azimuthal magnetic perturbation fields on spacecraft passes over the planet's polar regions. Passes at smaller radial distances are preferred due to the larger amplitudes of the perturbation fields and the rapidity of crossing the current layers resulting in near "snapshots" being obtained of the perturbations at fixed time. Such passes also penetrate to field lines located deeper within the inner magnetosphere, thus more fully characterizing the current system. As noted in section 1.1, the principal currents of both subcorotation and PPO systems extend inward to ~10 R_S in the equatorial plane, such that field-aligned current studies at Saturn require sufficiently inclined orbits with near-periapsis equatorial crossings within ~10 R_S to provide adequate coverage of the main currents.

Properties of Cassini's orbit around Saturn are shown in Figure 2 over an 11-year interval from the start of 2005 to the end of 2015, in order to identify intervals during which such studies are feasible. Time in days is shown at the bottom of the figure, where $t = 0$ corresponds to 00 UT on 1 January 2004, while year boundaries are shown in red at the top of the figure. The times of Cassini periapsides are shown by black tick marks at the top of figure and marked with revolution (Rev) orbit numbers, defined from apoapsis to apoapsis, every 10 Revs. Saturn vernal equinox is marked by the vertical red dashed line, separating postsolstice southern summer conditions from presolstice northern spring (see section 1.3). Figure 2a shows the latitude range on each Rev (black lines), plotted at the time of periapsis, while the red and blue circles show the latitude of apoapsis and periapsis, respectively. Three principal intervals of highly inclined orbits are evident, the first spanning 2006/2007, the second 2008/2009, and the third 2012/2015. Data from the first of these intervals were studied by Talboys, Arridge, Bunce, Coates, Cowley, and Dougherty, (2009), Southwood and Kivelson (2009), and Hunt et al. (2016), while data from the second were studied by Talboys, Arridge, Bunce, Coates, Cowley, Dougherty, and Khurana (2009), Talboys et al. (2011), and Hunt et al. (2014, 2015), both intervals corresponding to late southern summer. Here we newly concentrate on data from the third interval, corresponding to northern spring.

Figure 2b shows the radial range of each Rev on a log scale, where the radial distance of periapsis is of relevance for reasons given above. During the first interval of inclined orbits periapsis was located well below ~10 R_S at the beginning and end of the interval but rose above this limit in the central part. Consequently, useful field-aligned current data were obtained in two intervals spanning Revs 30–36 during late 2006 and Revs 41–44 in early 2007, as shown by the vertical blue bars (e.g., Hunt et al., 2016). In the second interval, periapsis was sufficiently low during the early part of the interval spanning Revs 59–95 in 2008 (Hunt et al., 2014, 2015), as again shown by the blue bar, but subsequently also became too large. A similar pattern occurred during the third interval of highly inclined orbits, with sufficiently small periapsides occurring for Revs 168–194 in 2012/2013 as examined here, again marked by the blue bar, before also becoming too large. We note, however, that the periapsis distances on the 2012/2013 Revs, typically ~6–8 R_S, are rather larger than those of the 2008 prime comparator data set, typically ~3–5 R_S, such that by comparison the 2012/2013 passes are slower and penetrate less deeply into the inner magnetosphere.

Figure 2c shows the LT of apoapsis (red) and periapsis (blue) on each Rev. The LT of periapsis gives an initial indication of the LT of the spacecraft passes over the field-aligned current regions. During the late 2006 interval this was located near noon, moving sharply to predawn in early 2007, and then more slowly to the midnight sector in the 2008 interval. These data allowed Hunt et al. (2016) to compare southern hemisphere current signatures between midnight and dawn/noon LTs under late southern summer conditions. During the third interval periapsis was located in the postmidnight/predawn sector, similar to the second interval, thus allowing comparison of nightside currents under late southern summer and northern spring conditions as discussed here.

Figure 2d shows the orbit period of each Rev from apoapsis to apoapsis, plotted at the time of periapsis. During the third interval studied here, the period was initially ~20 days but subsequently decreased to ~10 days near the end of 2012, comparable to that during the 2008 interval.
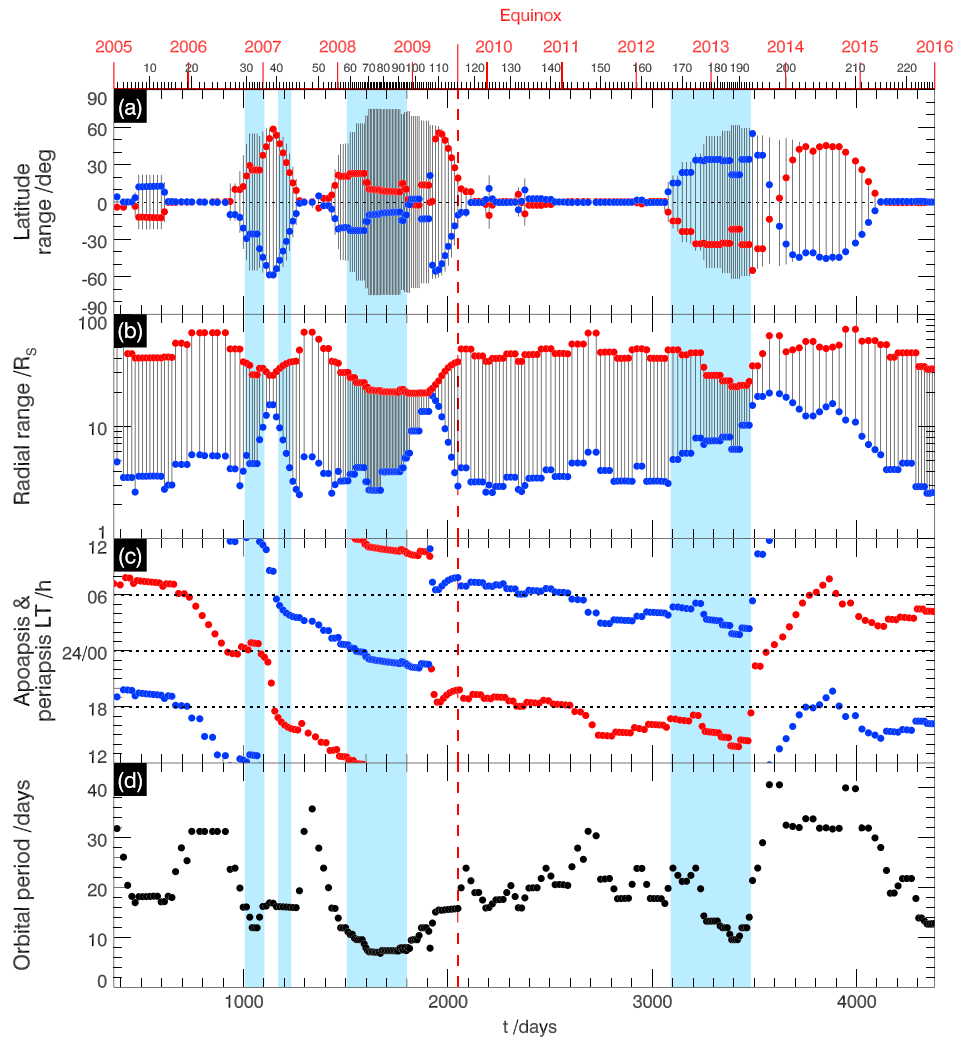
Figure 2. Overview of Cassini orbital parameters from 2005 to 2015 inclusive. Time is given at the bottom of the figure in days with $t = 0$ corresponding to 00 UT on 1 January 2004, while start of year markers are shown in red at the top. The vertical red dashed line marks Saturn vernal equinox in mid-August 2009. Each spacecraft Rev, defined from apoapsis to apoapsis, is indicated by black ticks at the top of the figure, plotted at the time of periapsis, with every tenth Rev being numbered. (a) The latitude range on each Rev (deg), plotted at the time of periapsis, with colored circles marking the latitude of periapsis (blue) and apoapsis (red). (b) The radial range on each Rev on a log scale (R_S), also plotted at the time of periapsis. (c) The local time, LT, (hours) of periapsis (blue) and apoapsis (red) for each Rev, plotted at the times corresponding to those events, where horizontal dotted lines indicate dusk (18 hr), midnight (24/00 hr), and dawn (06 hr). (d) The spacecraft orbit period for each Rev (days), plotted at the time of periapsis. The vertical blue shaded bands indicate intervals in which the spacecraft orbit allows adequate observation of field-aligned currents, the first closely spaced pair in 2006/2007, the second in 2008, and the third, that studied here, in 2012/2013.

1.3. Physical Conditions

Figure 3 shows physical parameters relevant to this study, plotted over the same interval as Figure 2. Figure 3a shows the latitude of the Sun at Saturn, indicative of Saturn's seasons, which passed through zero from southern summer to northern spring at vernal equinox in mid-2009. The prior southern solstice was in late 2002, and the following northern solstice in mid-2017. During the 2012/2013 interval studied here, again marked by the blue bar, the solar latitude increased from +15° to +19°, such that the northern atmosphere to ~17° northern colatitude was in permanent sunlight, while the southern ionosphere to ~17° southern colatitude was in permanent darkness. The opposite asymmetry occurred during the 2008 interval during which the solar latitude varied from −8° to −4°, such that the southern atmosphere to ~6° colatitude was in permanent sunlight, while the northern atmosphere to ~6° colatitude was in permanent darkness.

Figures 3b–3e show parameters of the northern (blue) and southern (red) PPO systems. Figure 3b shows the PPO periods, $\tau_{N,S}$, where values from 2005 to 2010 spanning equinox were derived from magnetic data by
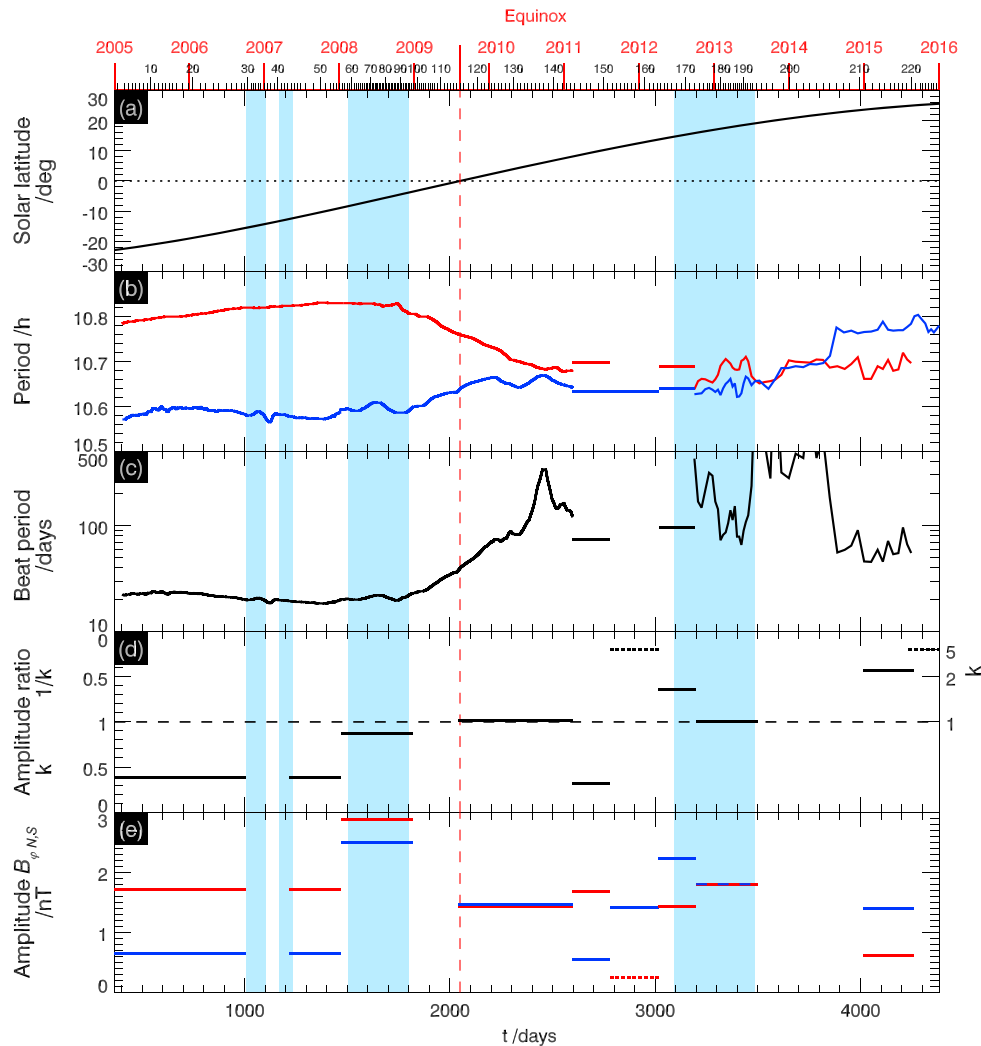
Figure 3. Physical conditions at Saturn shown in a similar format to Figure 2, and over the same interval. (a) The latitude of the Sun at Saturn (deg), passing through zero at vernal equinox marked by the vertical red dashed line. (b) The periods (hours) of the northern (blue) and southern (red) PPOs. (c) The PPO beat period (days) using a log scale. (d) The north/south amplitude ratio, k, of the two PPOs determined from beat phase modulation of the oscillation phases within the equatorial region when available, where k is plotted directly between 0 and 1 in the lower half plot and $1/k$ is plotted between 1 and 0 in the upper half plot (see also the k scale on the right). Dotted lines indicate intervals in which southern PPO modulations could not be discerned, indicating $k \geq 5$. (e) The amplitudes (nT) of the northern (blue) and southern (red) oscillations in the equatorial field region, specifically for the azimuthal field component. Where the two amplitudes are equal (i.e., $k = 1$), they are indicated by red and blue dashed lines.

Andrews et al. (2012), from 2011 to 2012 by Provan et al. (2013), and from 2013 to 2015 by Provan et al. (2016). During the first two high-latitude intervals the two periods were well separated at ~10.6 hr for the northern PPO system and ~10.8 hr for the southern. During the third interval studied here the periods were much closer at ~10.64 hr for the northern and ~10.69 hr for the southern, with the northern period still shorter than the southern. Directly after the end of the this interval, however, in mid-2013 the two periods coalesced for ~1 year and then reversed sense with the northern period longer than the southern after mid-2014.

Figure 3c shows the beat period, τ_B, of the two PPO oscillations plotted on a log scale, given by

$$\frac{1}{\tau_B} = \left| \frac{1}{\tau_N} - \frac{1}{\tau_S} \right|. \tag{1}$$

For the first two high-latitude intervals (2006/2007 and 2008) the beat period was relatively short at ~20 days, compared with an orbit period of ~10 days (Figure 2d), such that successive passes typically occurred at

intervals of a half of a beat period. For the third high-latitude interval (2012/2013), however, due to the smaller separation of the periods the beat period increased to ~100 days compared with the orbit period of ~10–20 days, such that successive passes occurred at intervals of a tenth to a fifth of a beat period. Even so, approximately four beat cycles were completed over the whole interval of study, such that the full range of relative phase conditions between the two PPO systems was experienced.

Figure 3d shows the north/south amplitude ratio, k, of the two PPO oscillations determined from beat phase modulation of the oscillation phases within the quasi-uniform perturbation field region where the two PPO oscillations are superposed (e.g., Andrews et al., 2012; Provan et al., 2013, 2014, 2016). (Observations in the quasi-dipolar regimes cannot be used for this purpose since no model of the polar amplitude variation, e.g., with radial distance, has yet been devised.) Parameter k is plotted directly in the range $0 \leq k \leq 1$ in the lower half of the plot, while $1/k$ is plotted in the range $1 \geq /k \geq 0$ in the upper half, thus uniformly covering the full range of k from 0 to infinity. Dotted lines indicate intervals in which southern PPO modulations could not be discerned in these data, indicating $k \geq 5$ (Provan et al., 2013). During southern summer the southern PPO was dominant by a factor of ~2.5, with the two oscillations becoming near equal in amplitude in the trans-equinoctial interval between 2008 and 2011 (Andrews et al., 2012).

Postequinox, the values become more variable over ~100 to 200 day intervals of southern dominant, northern dominant, and near-equal amplitude oscillations, before becoming clearly northern dominant soon after the start of 2015 during the interval of reversed periods. In the second and third high-latitude intervals of primary interest here the oscillations were of near-equal amplitude in both cases, being slightly southern dominant with $k \approx 0.87$ in 2008 and slightly northern dominant with $k \approx 1.6$ falling to $k \approx 1.0$ in 2012/2013. These values were both determined from beat modulation of unfiltered azimuthal field data obtained during the rapid near-periapsis equatorial passes on these highly inclined Revs (Andrews et al., 2012; Provan et al., 2016). Individual amplitudes of the equatorial azimuthal field oscillations are plotted in Figure 3e, showing that these decreased between the second and third high-latitude intervals, by a factor of ~0.7 for the northern system and ~0.6 for the southern system. The PPO-related currents may also be expected to be less by similar factors.

## 2. Data Set and Analysis Procedures

2.1. Data Set

As discussed in section 1, the data set analyzed here consists of 1-min averaged values of the azimuthal magnetic field, B_φ, obtained on the periapsis passes of Cassini Revs 168–194 between mid-2012 and mid-2013, corresponding to the central interval of Saturn northern spring. Since data from Rev 172 are missing due to an extended trans-periapsis data gap, this gives a set of 26 passes across both northern and southern field-aligned current regions. However, as in previous studies of the 2008 data by Hunt et al. (2014, 2015), initial examination shows that the northern passes on Revs 173 and 182 and the southern pass on Rev 169 show atypical signatures, such that these have been excluded from further analysis. The data from the three excluded passes are briefly examined in Appendix A and compared with the included data in Figure A1. They are taken to represent cases of the occurrence of relatively short-lived (one ~1 day pass or less) unusual dynamic activity taking place in the magnetosphere on these passes, such as the effects of auroral storms associated with strong magnetospheric compressions by the solar wind (e.g., Bunce et al., 2010). Overall, the data set employed here thus consists of 24 northern and 25 southern polar passes. This compares with 34 northern and 31 southern passes in the 2008 data set (Hunt et al., 2014, 2015).

Figure 4 shows the trajectories of three representative Revs from the beginning (170, blue), middle (180, green), and end (190, red) of the interval examined here. Specifically, Figures 4a–4c show the trajectories projected onto the *X-Z*, *Y-Z*, and *X-Y* planes in Kronographic Stationary (KGS) coordinates, respectively, where *Z* is Saturn's spin/magnetic axis, the *X-Z* plane contains the Sun (directed to the right in Figures 4a and 4c), and *Y* completes the right-hand system pointing toward dusk. Solid circles show start of day time marks, numbered with time in days as in Figures 2 and 3. To convert to day of year in 2012 or 2013 as appropriate, we note that the start of day of year 1 in 2012 corresponds to 2,922 days, while the start of day 1 in 2013 corresponds to 3,288 days (dates are also provided in the figure caption). The spacecraft passed inbound in the premidnight sector of the southern hemisphere to reach periapsis at ~6–8 R_S in the postmidnight sector of the northern hemisphere, before passing outbound via dawn in the northern hemisphere (see also Figures 2b and 2c).
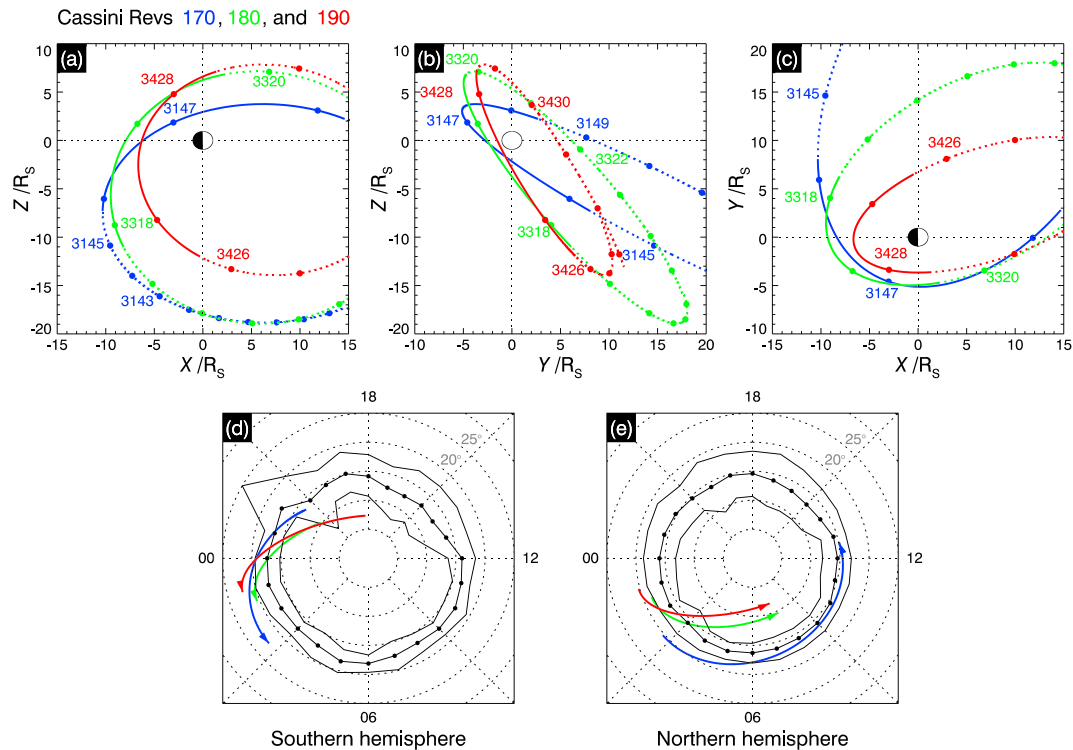
Figure 4. Trajectories of representative Cassini Revs projected onto (a) the *X-Z* plane, (b) the *Y-Z* plane, and (c) the *X-Y* plane in planetocentric KGS coordinates, where *Z* is aligned with Saturn's spin/magnetic axis (positive north), the *X-Z* plane contains the Sun (*X* pointing sunward), and *Y* completes the right-handed triad (pointing duskward). Three Cassini Revs (170, 180, and 190) are shown, color coded as shown at the top of the figure, where the solid portions of the trajectories show the intervals from which data have been employed in the study. Solid circles are start of day markers, labeled with the time (days) since 00 UT on 1 January 2004. The dates corresponding to the first numbers shown on each trajectory correspond to the start of 9 August 2012 for Rev 170, 31 January 2013 for Rev 180, and 19 May 2013 for Rev 190. (d and e) The three Revs projected along model field lines into the southern and the northern ionospheres, respectively, where only the solid line portions of the trajectories are shown. Arrows indicate the direction of travel. Both ionospheres are viewed from the north (through the planet for the southern ionosphere), with noon on the right and dusk at the top. Latitude circles are shown as dotted circles at 5° intervals. The statistical position of the auroral oval determined by Carbary (2012) from Cassini Ultraviolet Imaging Spectrograph data is also shown, where black circles joined by black lines show the position of maximum power at 1-hr intervals of local time, while the black lines on either side show the half-power points.

The solid line segments of the trajectories in Figures 4a–4c show the intervals from which data have been employed, the criteria for which are discussed below. In Figures 4d and 4e these segments are projected along model field lines into both the southern (Figure 4d) and northern (Figure 4e) ionospheres, with noon at the right and dusk at the top. The view of the southern hemisphere in Figure 4d is through the planet from the north. The break point between the two mappings lies at the near-periapsis point where the trajectory is tangent to the model flux shells, such that the mapped footprints then lie at the largest colatitudes from the poles in both hemispheres. As in Hunt et al. (2014, 2015), the model field employed is axisymmetric, consisting of the three-term internal planetary field model of Burton et al. (2010), together with the empirical ring current model of Bunce et al. (2007) for a typical subsolar magnetopause distance of 22 R_S. The ionosphere is taken to lie 1,000 km above the International Astronomical Union (IAU) 1-bar Saturn reference spheroid (e.g., Galand et al., 2011), the polar and equatorial radii of the 1-bar spheroid being 54,364 and 60,268 km, respectively. Also shown are the average locations of the auroral regions both north and south, as determined from Cassini Ultraviolet Imaging Spectrograph data by Carbary (2012), where the central line with black circles at each LT hour shows the colatitude of maximum intensity, while the lines on either side show the half-maximum intensity points. Figure 4d shows that inbound the spacecraft crossed southern auroral field lines centered near ~17.5° southern colatitude (where the main upward currents flow) in the premidnight and midnight sectors. Figure 4e shows that outbound it crossed northern auroral field lines at ~16° northern colatitude in the postmidnight and dawn sectors. The difference in colatitude between the two hemispheres is due to the axial quadrupole asymmetry of the internal field. For the 2008 data set the southern auroral trajectory projections are close to midnight and postmidnight, similar to Figure 4d, while the
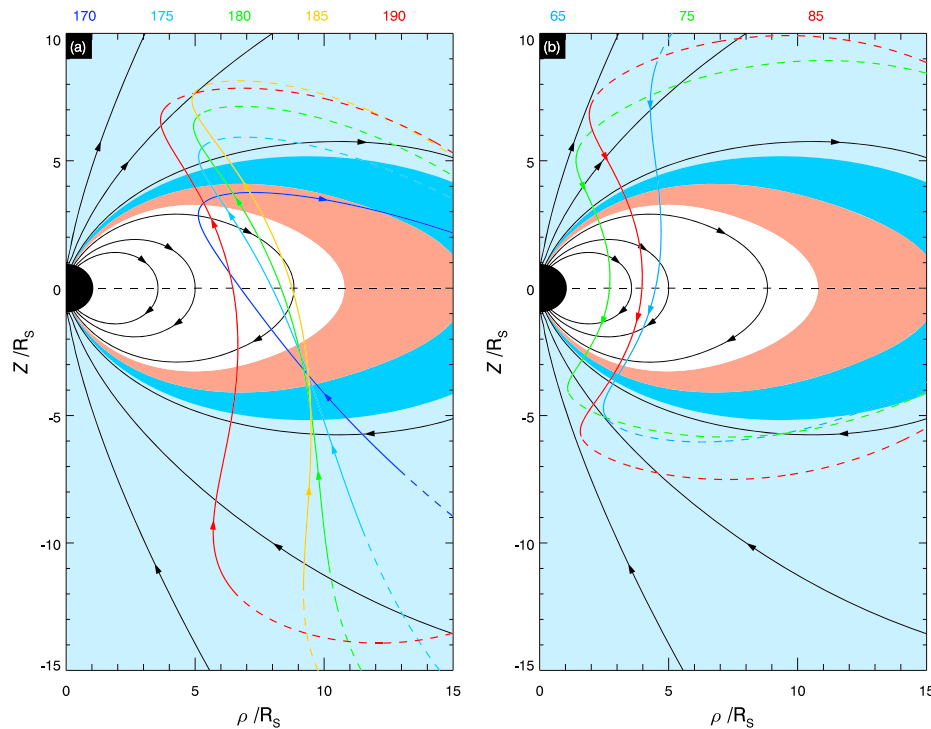
Figure 5. Trajectories of representative Cassini Revs plotted in cylindrical (ρ,Z) coordinates, where Z is Saturn's spin/magnetic axis (positive north) and ρ is the perpendicular distance from this axis. (a) Revs from 2012/2013 and (b) Revs from 2008 as studied by Hunt et al. (2014, 2015). Trajectories are color coded as shown at the top of each figure, with arrows indicating the direction of travel. As in Figure 4 the solid line segments indicate intervals from which data have been employed in the corresponding studies. Black arrowed lines show model field lines plotted at intervals of 5° southern ionospheric colatitude (up to 30°), while field-aligned shading indicates the approximate regions of principal field-aligned current flow associated with the southern subcorotation current system determined by Hunt et al. (2014). The pale blue areas indicate polar regions of distributed downward currents on open field lines typically bounded by the open-closed boundary (Jinks et al., 2014), the darker blue areas show the enhanced downward current regions typically lying just equatorward of the open-closed boundary, and the red area the principal upward current region mapping to the auroral oval. The principal PPO currents map to the dark blue and red regions on closed field lines.

northern projections are displaced to the duskside of midnight in a manner similar to the dawn displacements in Figure 4e (see Hunt et al., 2015, their Figures 2c and 2d). Overall, however, the 2008 and 2012/2013 passes are sufficiently similar in nature that direct comparison is appropriate.

Figure 5 provides further comparison, where representative Revs are shown in cylindrical (ρ,Z) coordinates, where Z is again distance along Saturn's spin/magnetic axis and ρ is the perpendicular distance from that axis. Arrowed black lines show the field lines of the magnetic model, plotted at 5° ionospheric colatitude intervals from the southern pole to 30° (~3.6 R_S in the equatorial plane). The colored areas, also bounded by field lines, indicate the approximate locations of principal field-aligned current regimes, specifically those of the southern subcorotation system found by Hunt et al. (2014). Pale blue areas show the polar downward current regions (Figure 1b), the darker blue bands the region of enhanced downward current mapping from near the OCB to ~15.5° and 17° in the northern and southern ionospheres respectively, and the red shaded area the main upward current region mapping to ~17° and 19° in the northern and southern ionospheres, respectively (extending in to ~10 R_S in the equatorial plane). The main PPO currents also flow in the darker blue and red regions (Figures 1f and 1i).

Figure 5a shows the trajectories of five Revs from the 2012/2013 data set (including those in Figure 4) superposed on these field regimes, while Figure 5b similarly shows representative trajectories from 2008. Each Rev is color coded as shown at the top of each panel, with the solid line segments showing where data were employed for analysis. As in Hunt et al. (2014, 2015), this is primarily defined by the trans-periapsis segment lying between the two points with the smallest mapped colatitudes in the two hemispheres, that is, the points where the trajectory in the ρ-Z plane is tangent to the polar field lines. For the 2012/2013 data set we have also applied a limiting radial distance of 15 R_S, corresponding approximately to the outer limit of where the model field, dominated by the internal field, is likely to be reasonably accurate, representing a

radius roughly half way to the magnetopause in the dayside magnetosphere. This limiting distance was not exceeded on any pass in the 2008 data set but applies to a few of the earlier Revs in the 2012/2013 interval as seen in Figure 5a.

Figure 5a shows that the 2012/2013 Revs provide relatively straightforward cuts through the main field-aligned current regions, as for the 2008 data set, except perhaps for the early Revs in the northern hemisphere. However, the larger periapsis distances for the 2012/2013 data set imply slower crossings than for the 2008 data set, the consequences of which will be shown in section 2.3. With crossings further from the ionosphere, the ionospheric currents deduced from the field data may also be overestimated or underestimated if there are significant cross-field currents flowing between the ionosphere and the point of observation (Figures 1b, 1e, and 1h). However, much of the cross-field current is expected to flow closer to the equator where the bulk of the plasma mass is located, far from the field-aligned current crossing points. In particular, in the equatorial regions of these Revs at radial distances of ~6–9 R_S, most of the plasma mass (and hence any cross-field current) is expected to be confined to within ~1 R_S of the equatorial plane (Persoon et al., 2009, 2013).

2.2. Data Analysis Procedures

Analysis of the B_φ data from 2012/2013 follows that in the related studies by Hunt et al. (2014, 2015), such that only a brief outline will be given. First, we estimate and remove the generally small contributions to B_φ that are not due to field-aligned currents. Since Saturn's internal and inner ring current fields are closely axisymmetric (Burton et al., 2010; Kellett et al., 2011), these fields are expected to be due principally to the tail and magnetopause currents. As in previous studies, these have been estimated on the Cassini trajectory using the paraboloid model of Saturn's magnetosphere (see, e.g., Alexeev et al., 2006), specifically using the "intermediate" model of Belenkaya et al. (2008) for a subsolar magnetopause distance of 22 R_S. These fields have then been subtracted from the observed values, such that all subsequent analysis uses the "corrected" values. However, the subtracted fields are generally small compared with the observed field (section 2.3), such that this procedure has only a modest effect on the results.

The corrected azimuthal field is then mapped along field lines into the appropriate ionosphere and the meridional current at the feet of the field lines estimated (Figure 1). To do this, we assume that ρB_φ is constant along field lines (ρ again being perpendicular distance from the spin/magnetic axis), an approximation that is exact for axisymmetry and in the absence of cross-field current flow on the field line extending between the observation point and the ionosphere. Hunt et al. (2014) showed that the approximation should also be valid for sheet-like currents such as those considered here, where the latitude scale is much smaller than the longitude scale. The azimuthal field just above the ionosphere, $B_{\varphi i}$, is then given by

$$B_{\varphi i} = B_\varphi \left(\frac{\rho}{\rho_i} \right), \tag{2}$$

where ρ_i is the perpendicular distance of the foot of the field line in the ionosphere. Ampère's law then gives the meridional (mainly Pedersen) current per radian of azimuth in the ionosphere at the feet of the field lines which switches off the azimuthal field under the ionosphere, I_m, as

$$I_m = \mp \frac{\rho_i B_{\varphi i}}{\mu_0} = \mp \frac{\rho B_\varphi}{\mu_0}, \tag{3}$$

where μ_0 is the permeability of free space. The upper and lower signs correspond to the northern and southern hemispheres, respectively, and I_m is taken positive when directed toward the equator in both hemispheres. Again, assuming that longitude variations can be neglected, current continuity requires that field-aligned currents flow into and out of the ionosphere as I_m varies with colatitude. For meridional currents at colatitudes θ_1 and θ_2 with respect to either pole, $\theta_2 > \theta_1$, the amount of field-aligned current flowing between the two locations, $I_\parallel$, is given by

$$I_\parallel = -(I_m(\theta_2) - I_m(\theta_1)), \tag{4}$$

where negative values indicate downward currents in both hemispheres and positive values upward currents. Thus, if $I_m(\theta_2) < I_m(\theta_1)$, net field-aligned current flows out of the ionosphere between these two points, while if $I_m(\theta_2) > I_m(\theta_1)$, net field-aligned current flows into the ionosphere between them. The field-
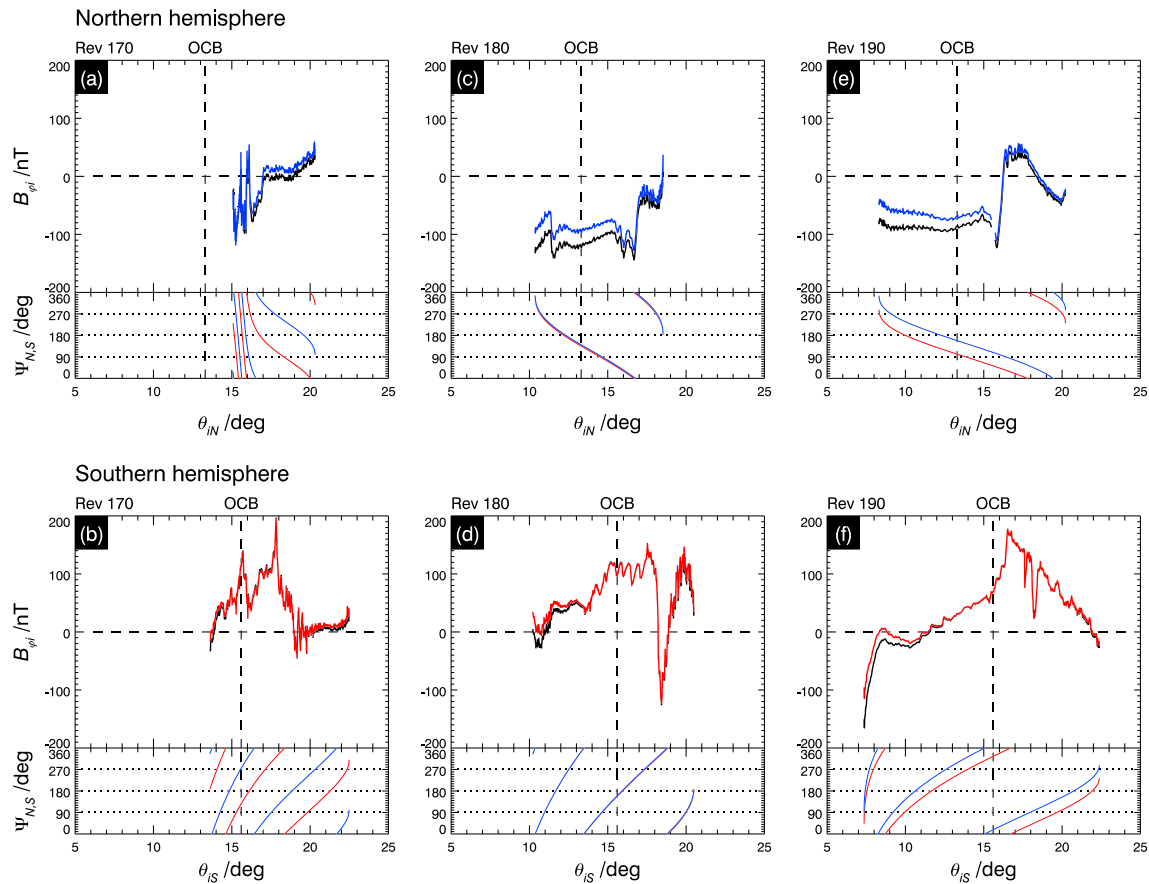
Figure 6. Representative azimuthal field data from three Revs, Revs 170 (a and b), 180 (c and d), and 190 (e and f), the trajectories of which are shown in Figures 4 and 5a. In the upper panels of Figures 6a, 6c, and 6e data obtained from north of the planetary equator are projected along model field lines into the northern ionosphere using equation (2) and plotted versus northern ionospheric colatitude θ_{iN}, while in the upper panels of Figures 6b, 6d, and 6f data from south of the planetary equator are similarly projected into the southern ionosphere and plotted versus southern ionospheric colatitude θ_{iS}. Black data show the fields derived directly from the azimuthal field as measured, while the blue (northern) and red (southern) data show the fields after subtraction of the magnetospheric contribution estimated using the paraboloid field model, as discussed in the text. Vertical dashed lines indicate the position of the northern and southern OCB (Jinks et al., 2014). The lower parts of the figures show the corresponding phases of the northern (blue) and southern (red) PPO systems at the spacecraft, $\Psi_{N,S}$ modulo 360°, given by equation (5).

aligned current then remains fixed on a given flux tube (such that $(j_\parallel/B)$ = constant, where $j_\parallel$ is the current density) in the region between the ionosphere and the magnetospheric closure currents.

2.3. Representative Examples

The procedures in section 2.2 result in the estimation of colatitude profiles of $B_{\varphi i}$ (and hence I_m) in both northern and southern hemispheres on each pass. Figure 6 shows examples for the representative Revs in Figure 4. Figures 6a and 6b show the northern and southern profiles for Rev 170 plotted versus northern and southern colatitude, respectively, similarly Figures 6c and 6d for Rev 180, and Figures 6e and 6f for Rev 190. Vertical dashed lines show the averaged OCB location as found by Jinks et al. (2014), at 13.3° colatitude in the northern hemisphere and 15.6° in the southern hemisphere. In the upper panels the black lines show the azimuthal field as mapped to the ionosphere using equation (2), while the colored lines, blue in the north and red in the south, show the profiles after removal of the estimated magnetospheric contribution, as discussed in section 2.2. The effect is seen generally to be small, though the differences increase with distance away from the noon-midnight meridian.

The lower panels in Figures 6a–6f show the northern and southern PPO phases, Ψ_N (blue) and Ψ_S (red) as determined from analysis of the PPO perturbation fields observed in the near-equatorial and polar regions by Provan et al. (2013, 2016). The analysis yields a model of $\Phi_{N,S}(t)$, the azimuthal angle of the $\Psi_{N,S} = 0°$
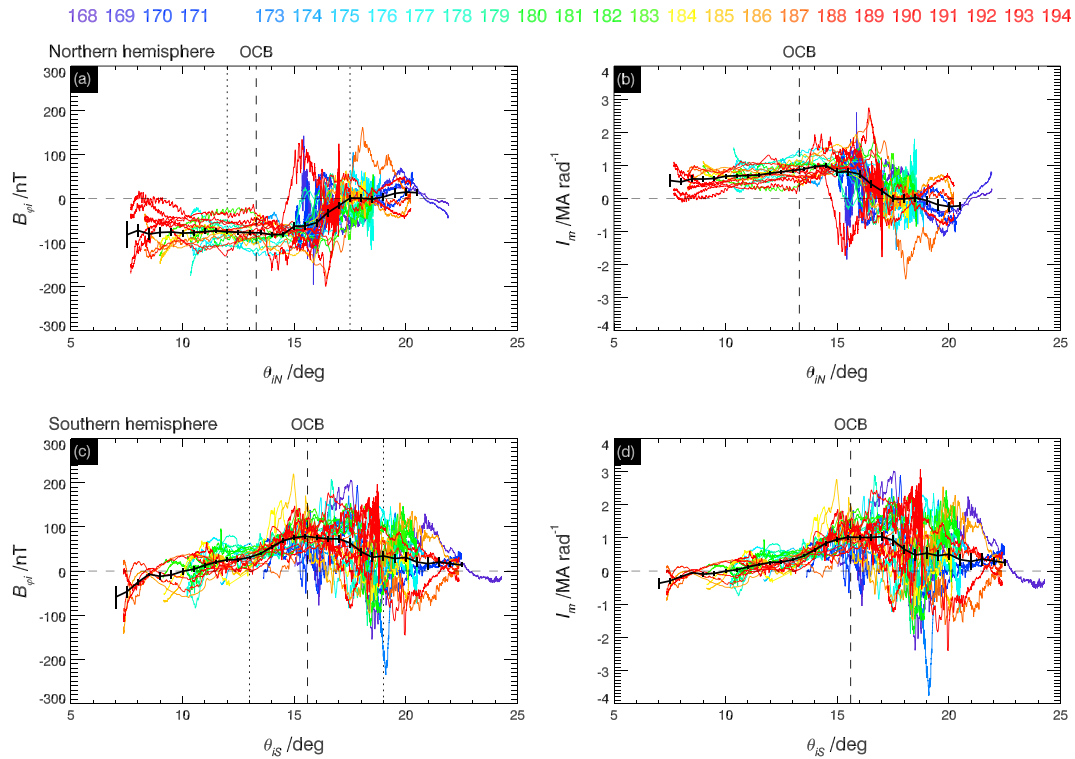
Figure 7. Composite plots showing mapped ionospheric azimuthal field $B_{\varphi i}$ (nT) and meridional current I_m (MA rad^{-1}) data from all the Revs in the 2012/2013 interval included in this study, color coded as shown at the top of the figure (consistent with Figures 4 and 5). (a and c) $B_{\varphi i}$ for the northern and southern hemisphere data, respectively, plotted versus the corresponding northern and southern ionospheric colatitudes $\theta_{iN,S}$ (deg). (b and d) I_m for the northern and southern hemispheres, respectively. Black lines overplotted on the data show mean values computed in overlapping 1° colatitude bins at intervals of 0.5° (see details in the text), shown only when there are at least three contributing Revs. Black error bars show the standard error of the mean. Vertical black dashed lines show the averaged location of the open-closed boundaries in the northern and southern hemispheres (Jinks et al., 2014), while the vertical black dotted lines in Figures 7a and 7c show the colatitude boundaries employed in Figure 8.

meridians (see Figures 1d and 1g) measured from noon in the sense of planetary rotation. The northern and southern phases in Figure 6 are then given by

$$\Psi_{N,S}(\varphi, t) = \Phi_{N,S}(t) - \varphi, \tag{5}$$

where φ is the azimuth of the spacecraft relative to noon, also measured in the sense of planetary rotation. The PPO phases are seen to vary significantly on a given pass, related to significant variations of the observed azimuthal field equatorward of the OCB, such that as indicated in section 2.1, individual profiles do not approximate to snapshots of the field at a given time. As in the study by Bunce et al. (2014), the varying PPO phase on a given pass must thus be taken into account. These phase plots also illustrate the varying PPO beat phase conditions encountered, with near antiphase for Rev 170, near in phase for Rev 180, and near quadrature for Rev 190.

3. Analysis of the 2012/2013 High-Latitude Data Set

3.1. Overview of Field and Current Colatitude Profiles

Figure 7 provides an initial overview of the systematics and variability of the data set, where colatitude profiles of the ionospheric azimuthal magnetic field (corrected values as in all subsequent figures) and derived meridional current profiles are shown for all the 2012/2013 data included in the study, selected as described in section 2.1. Data from each Rev are color coded as shown at the top of the figure. Specifically, Figures 7a and 7b show the northern hemisphere $B_{\varphi i}$ (equation (2)) and I_m (equation (3)) data, respectively, plotted versus northern colatitude θ_{iN}, while Figures 7c and 7d show the southern hemisphere $B_{\varphi i}$ and I_m data, respectively, plotted versus southern colatitude θ_{iS}. The averaged position of the OCB in each hemisphere is shown
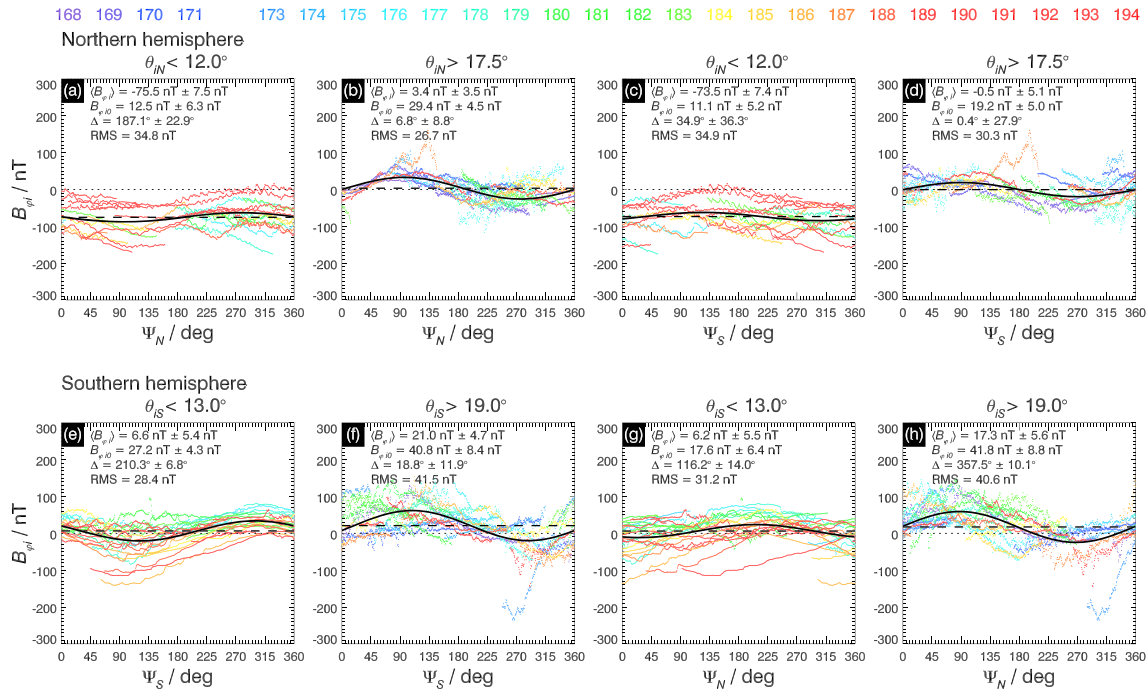
Figure 8. Examination of the dependence of the polar and equatorial ionospheric azimuthal fields $B_{\varphi i}$ (nT) in the northern and southern hemispheres on the northern and southern PPO phases $\Psi_{N,S}$ (deg). The polar and equatorial regions are those defined by the vertical dotted lines in Figures 7a and 7c, corresponding to $\theta_{iN} \leq 12°$ and $\theta_{iN} \geq 17.5°$, respectively, in the northern hemisphere, and $\theta_{iS} \leq 13°$ and $\theta_{iS} \geq 19°$, respectively, in the southern hemisphere. (a and c) The northern polar data plotted versus the northern and southern phases, respectively, and (b and d) the northern equatorial data similarly plotted versus the two phases. (e and g) The southern polar data plotted versus the southern and northern phases, respectively, and (f and h) the southern equatorial data similarly plotted versus the two phases. The data from each Rev are color coded as shown at the top of the figure. Black solid lines show sinusoidal fits given by equation (6), with the mean value $\langle B_{\varphi i} \rangle$ being shown by the horizontal black dashed line. Fit parameters together with the root-mean-square (RMS) deviation are given in the upper left of each figure.

by vertical dashed lines (Jinks et al., 2014), while the pairs of vertical dotted lines in Figures 7a and 7c indicate the boundaries of the polar and equatorial regions employed in Figure 8 (section 3.2).

Overall, the azimuthal fields are seen generally to be negative in the north and positive in the south, indicative of lagging fields and subcorotation flows, though with major variability in the auroral region equatorward of the OCB leading to intervals with leading fields associated with supercorotating flows with respect to the planet's upper atmosphere. As discussed further below, the mean values of these data shown by the black lines provide an initial estimate of the subcorotation-related (PPO-independent) fields and currents in each hemisphere. The variations about the means also provide an indication of the amplitude of the PPO effects, which are seen to be comparable in magnitude. Other sources of variability are no doubt present as well, particularly at smaller spatial scales, but have been mitigated by the exclusion of atypical field/current profiles as discussed in section 2.1 and Appendix A.

If the PPO-related fields vary approximately sinusoidally with the PPO phases $\Psi_{N,S}$ as discussed in section 1.1, they will cancel near to zero at a particular colatitude given good phase coverage in the overall data set. As indicated above, the mean values of the data shown by the black lines in Figure 7 thus provide an initial estimate of the subcorotation-related current profiles (as demonstrated in section 3.4). These means have been calculated in overlapping 1° colatitude bins at intervals of 0.5°, where the data from each contributing Rev were first averaged individually, and then the means taken of these Rev-averaged values. A mean value is not shown if a bin contains data from less than three Revs. The error bars show the standard error of the means of the contributing Rev-averaged values. Examining these mean values, it is seen that the rising values of the current with colatitude in both polar regions, peaking at ~1 MA rad^{-1} just equatorward of the OCB, implies the existence of downward directed field-aligned currents in these regions totaling ~6 MA in each hemisphere assuming axisymmetry. The same current then flows out of the ionosphere over the auroral regions equatorward of the OCB, with the meridional current reducing to near-zero mean values beyond ~18° in the northern hemisphere and ~20° in the

southern. In the two polar regions the current profiles are seen to be different, however, indicative of a broadly distributed downward current in the northern (summer) hemisphere, while the meridional currents remain small to within a few degrees of the OCB in the southern (winter) hemisphere, indicative of weak ionospheric conductivities, and then rise to similar values as in the northern auroral region due to a narrower ring of downward current. A similar polar region asymmetry was found by Hunt et al. (2015) in the 2008 data during southern summer conditions but reversed in sense between the two hemispheres (their Figure 3). These evidently seasonal asymmetries will be discussed further in sections 3.8 and 4.

3.2. PPO-Related Variations at Small and Large Colatitudes

We now examine the data in more detail for PPO-related variations, beginning by examining $B_{\varphi i}$ at small and large colatitudes, away from the main current sheets, where the mean values in Figure 7 do not vary greatly with colatitude. For the northern hemisphere we employ polar data from $\theta_{iN} \leq 12°$ and nearer-equatorial data from $\theta_{iN} \geq 17.5°$, while for the southern hemisphere we employ polar data from $\theta_{iS} \leq 13°$ and nearer-equatorial data from $\theta_{iS} \geq 19°$. The polar data correspond to regions of open field well poleward of the OCB in both cases. Results are shown in Figures 8a–8d for the northern hemisphere and in Figures 8e–8h for the southern hemisphere, where the data from each Rev are again color coded as shown at the top of the figure. Figures 8a and 8b show the northern polar and equatorial $B_{\varphi i}$ data, respectively, plotted versus northern PPO phase Ψ_N, while Figures 8c and 8d show the same data plotted versus the southern PPO phase Ψ_S in order to discern whether dual modulation is present. Figures 8e and 8f similarly show the southern polar and equatorial data, respectively, plotted versus southern PPO phase, while Figures 8g and 8h show the same data plotted versus northern PPO phase for similar purposes. We recall from section 1 that for the 2008 data Hunt et al. (2014, 2015) found dual modulation in the northern hemisphere data but not in the southern.

As discussed in section 1.1, we expect the PPO azimuthal field to vary as $+ \sin \Psi_{N,S}$ in the equatorial regions and as $- \sin \Psi_{N,S}$ on the opposite side of the field-aligned currents in the corresponding northern or southern polar regions. The black lines in Figure 8 show best fit sinusoids given by

$$B_{\varphi i} = B_{\varphi i} + B_{\varphi i0} \sin(\Psi_{N,S} - \Delta), \tag{6}$$

where the fit parameters are the mean value $\langle B_{\varphi i} \rangle$ (black dashed line), amplitude $B_{\varphi i0}$, and phase Δ. The fits were obtained by Levenberg-Marquardt least squares minimization (Markwardt, 2009), with fit parameters and root-mean-square (RMS) deviations being given in the upper left of each figure. Uncertainties were estimated using the "jackknife" statistical resampling method (section 4.1 of Hunt et al., 2015), where the circular standard deviation is given for phase Δ (Mardia & Jupp, 2000).

Examination of the polar data in Figures 8a and 8e shows PPO modulations close to the expected $- \sin \Psi_N$ forms in the northern hemisphere and $- \sin \Psi_{N,S}$ in the southern hemisphere (Δ close to 180° in both cases), though the northern modulations are weak compared, for example, with the ~30 nT amplitude of the corresponding southern polar oscillations in the 2008 data (Figure 5a of Hunt et al., 2015). Similar weak oscillations are derived when the northern polar data are plotted versus southern phase (Figure 8c) and the southern polar data versus northern PPO phase (Figure 8g), with phases Δ that do not correspond to simple physical expectation. Previous studies of the 2008 polar data by Andrews et al. (2012) and Hunt et al. (2015) did not detect modulation from the opposite hemisphere within a 10% limit by amplitude. For the near-equatorial data shown in Figures 8b, 8d, 8f, and 8h, however, clear dual modulation close to the expected $+ \sin \Psi_{N,S}$ form is seen in both hemispheres (Δ close to 0° modulo 360° in all cases), with the northern PPO modulation being stronger than the southern in the northern hemisphere, while the two modulations are near equal in amplitude in the southern hemisphere. However, if significant cross-field currents flow between the spacecraft and the corresponding magnetically conjugate ionosphere, particularly in the southern hemisphere due to the larger distances at which the auroral field lines are crossed (Figure 5a), the amplitudes in Figures 8b and 8f driven from the corresponding hemisphere could be underestimated, while those in Figures 8d and 8h driven from the opposite hemisphere could be overestimated. Nevertheless, these results show the presence of dual modulation on closed field lines in both hemispheres (see Figure 1), which must be taken into account in further analysis. Figure 8 also shows that there are no clear phase offsets between the equatorial and polar modulations in these data, unlike the ~35° offsets found in the 2008 data (Hunt et al., 2015).

3.3. Division of Data Into PPO "Phase Squares"

To determine the PPO dependency of the dual-modulated currents, we follow the procedure adopted by Hunt et al. (2015) to analyze the dual-modulated 2008 northern hemisphere currents but applied here to the data from both hemispheres. The data from each hemisphere are thus divided into non-overlapping 90° wide bins of northern and southern PPO phase, centered on $\Psi_{N,S}$ = 0°, 90°, 180°, and 270° (modulo 360°), each bin thus being ±45° about these values. We refer to these bins as phase squares, there being 16 in total for each hemisphere, corresponding to four northern phase bins times four southern phase bins. We then note that since the PPO-related modulations vary approximately as ± $\sin \Psi_{N,S}$ (Figure 8), northern system modulations should average near to zero in phase squares centered on Ψ_N = 0° and 180°, while southern system modulations should average near to zero in phase squares centered on Ψ_S = 0° and 180°. On the other hand, since the mean value of ± $\sin \Psi_{N,S}$ in the ±45° ranges about 90° and 270° is ± $\sin \Psi_{N,S}$ = ±$2\sqrt{2}/\pi \approx \pm 0.90$, northern system modulations should average close to the maximum and minimum values (actually ~90% thereof) in the phase squares centered on Ψ_N = 90° and 270°, while southern system modulations should average close to the maximum and minimum values in the phase squares centered on Ψ_S = 90° and 270°. Of course, in practice, these averages will depend in detail on the actual distribution of PPO phases within the data set, which Figures 7 and 8 indicate are in general broadly spread as required.

3.3.1. Northern Hemisphere Data

In Figure 9 we thus show northern colatitude profiles of the northern hemisphere meridional current in a similar format to Figure 7b but now separated into the 16 phase squares described above, arranged in four rows of four panels that display the effects of individual current components as outlined below. Due to the relatively slow traversals of the polar field lines, these profiles typically consist of short data segments from multiple Revs (color coded as in Figures 7 and 8). Despite this and the consequent data scatter, the data set is evidently sufficient to approximately define most of the current profiles in each phase square. As in Figure 7, mean values are computed in overlapping 1° colatitude bins every 0.5° (black lines and circles) by first averaging the data from each contributing Rev in each bin and then taking the mean of these Rev-averaged values. Means are plotted in the figure when there are at least two contributing Revs in a bin.

Figures 9a–9d (first row) show data from the four phase squares for which both Ψ_N = 0° or 180° and Ψ_S = 0° or 180° (as marked in the top right corners of each figure), such that the effects of both northern and southern PPO systems should average near to zero. The mean profiles in these figures thus represent four estimates of the northern hemisphere subcorotation current profile. Similar to Figure 7b, these show overall increasing values with northern colatitude in the polar region, followed by a sharp fall to near zero across ~15° to ~18° northern colatitude. Figures 9e–9h (second row) show data from the four phase squares for which Ψ_S = 0° or 180° such that the effects of the southern PPO system should average near to zero, but where Ψ_N = 90° (Figures 9e and 9f) or 270° (Figures 9g and 9h). These should then show equal and opposite effects of the northern PPO currents superposed on the subcorotation current. It can be seen that the profiles in Figures 9e and 9f for Ψ_N = 90° both extend to negative (supercorotation) values at larger colatitudes, while those in Figures 9g and 9h for Ψ_N = 270° remain positive (subcorotation) in the same colatitude range, this corresponding to the effect of the northern PPO currents expected from Figure 1f. Similarly, Figures 9i–9l (third row) show data from the four phase squares for which Ψ_N = 0° or 180° such that the effects of the northern PPO system should average near to zero, but where Ψ_S = 90° (Figures 9i and 9j) or 270° (Figures 9k and 9l), which should show equal and opposite effects of the southern PPO currents superposed on the subcorotation current. Again, it is seen that the currents for Ψ_S = 90° in Figures 9i and 9j extend to negative values at larger colatitudes while remaining positive for Ψ_S = 270° in Figures 9k and 9l, thus exhibiting the effect of the southern PPO current system expected from Figure 1f. These profiles thus confirm the dual modulation of the northern hemisphere currents by the two PPO systems. Figures 9m–9p (fourth row) show the final set of four phase squares for which both Ψ_N = 90° or 270° and Ψ_S = 90° or 270°, such that near maximum/minimum effects of both PPO systems should simultaneously be present, either in phase with each other (Figures 9m and 9n), then showing similar PPO-related effects to those just described, or in antiphase (Figures 9o and 9p) where they part cancel.
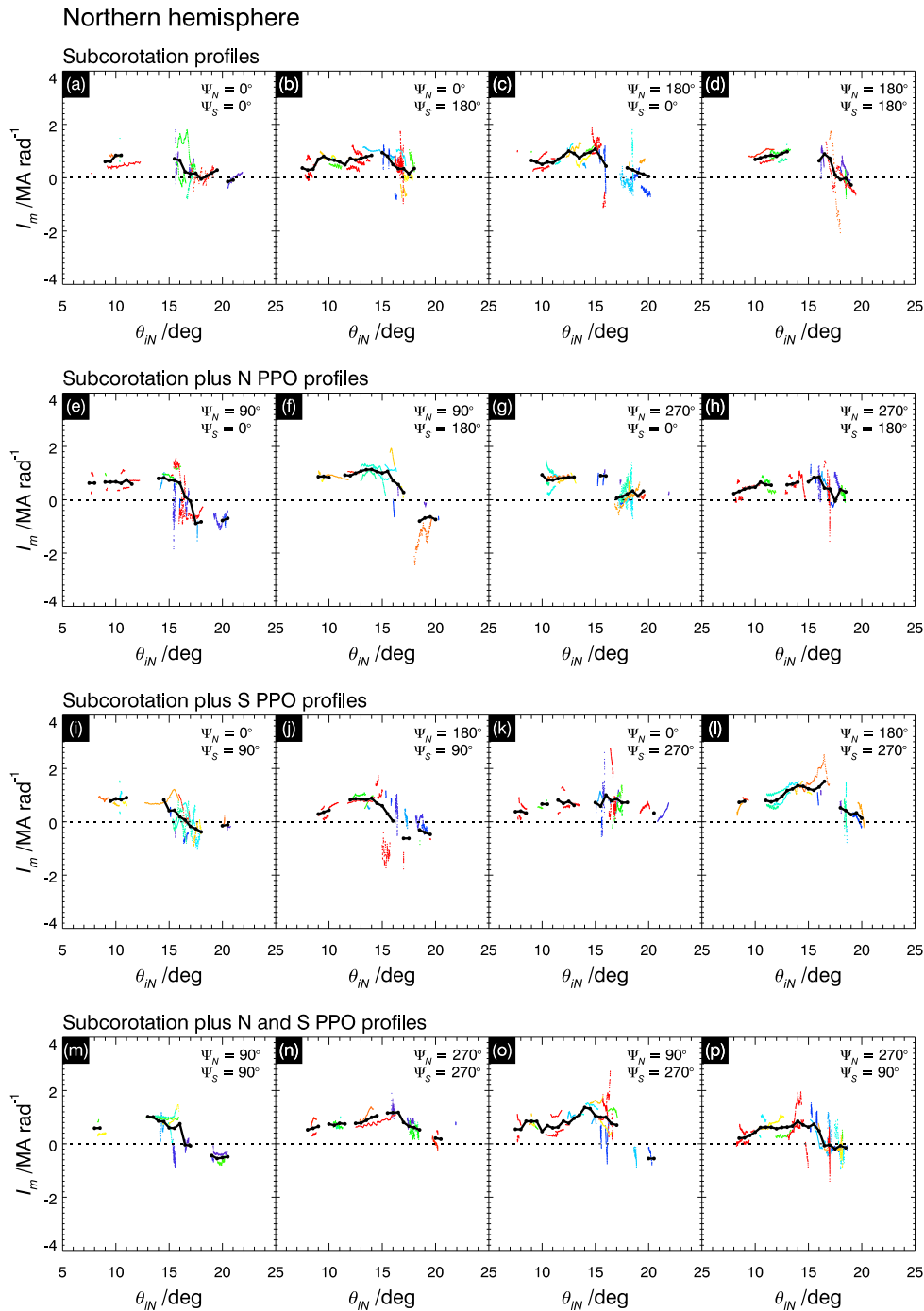
3.3.2. Southern Hemisphere Data

Figure 10 similarly shows southern colatitude profiles of the southern hemisphere meridional current divided into 16 nonoverlapping phase squares, as in Figure 9. Figures 10a–10d (first row) show four estimates of the subcorotation current similar to the mean profile in Figure 7c. Figures 10e–10h (second row) show the

Figure 9. Northern hemisphere meridional current per radian of azimuth I_m (MA rad^{-1}) data, derived from northern hemisphere mapped azimuthal magnetic field data (equation (3)), are shown separated into 16 nonoverlapping phase squares of northern and southern PPO phases I_m Ψ_N and Ψ_S (deg) and plotted versus northern ionospheric colatitude θ_{iN} (deg). The phase squares are 90° wide centered on the values indicated in the upper right corners of each figure. Data from each Rev are color coded as shown at the top of the figure (as in Figures 7 and 8), while black circles with black lines show mean values (see text) in overlapping 1° colatitude bins computed every 0.5° (shown when at least two Revs contribute to a bin). (a–d) Phase squares for which both northern and southern PPO currents are expected to average near to 0 ($\Psi_{N,S} = 0°$ or 180°), thus corresponding to subcorotation currents only. (e–h) Phase squares for which the northern but not the southern PPO currents are expected to contribute, $\Psi_N = 90°$ with $\Psi_S = 90°$ or 180° (Figures 9e and 9f) and $\Psi_N = 270°$ with $\Psi_S = 0°$ or 180° (Figures 9g and 9h). (i–l) Phase squares for which the southern but not the northern PPO currents are expected to contribute, $\Psi_S = 90°$ with $\Psi_N = 0°$ or 180° (Figures 9i and 9j) and $\Psi_S = 270°$ with $\Psi_N = 0°$ or 180° (Figures 9k and 9l). (m–p) Phase squares for which both the northern and the southern PPO currents are expected to contribute, either in phase with each other $\Psi_{N,S} = 90°$ or 270° (Figures 9m and 9n) or antiphase (Figures 9o and 9p).
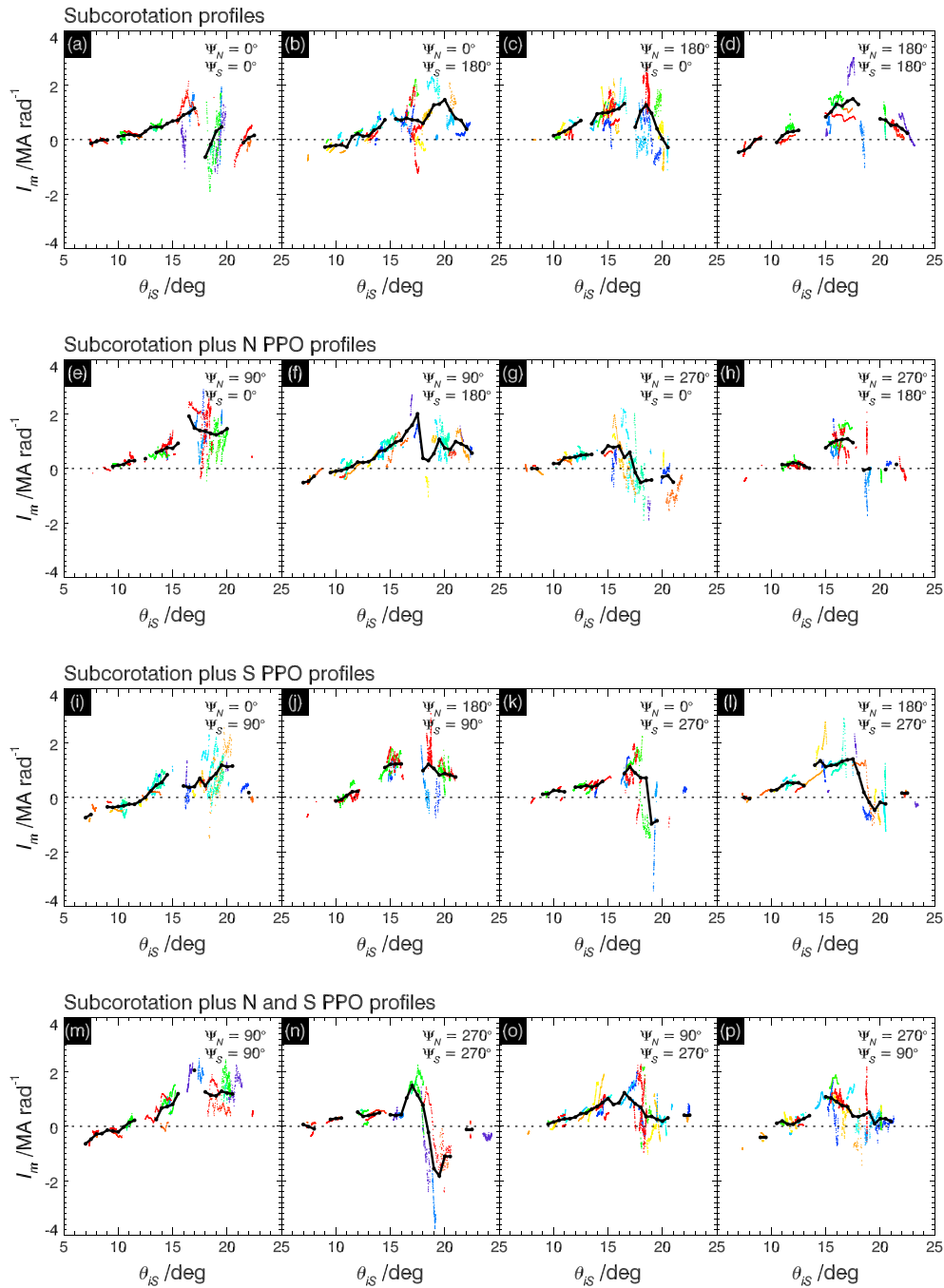
Figure 10. Southern hemisphere meridional current I_m (MA rad^{-1}) data, derived from southern hemisphere mapped azimuthal magnetic field data (equation (3)), are shown separated into 16 nonoverlapping phase squares of northern and southern PPO phases Ψ_N and Ψ_S (deg) and plotted versus southern ionospheric colatitude θ_{iS} (deg). The format is the same as Figure 9.

superposed effect of the northern PPO system in the expected averaged absence of the southern system, while Figures 10i–10l (third row) similarly show the superposed effect of the southern PPO system in the expected averaged absence of the northern system. These profiles again show PPO-related modulations, most evidently at larger colatitudes, where the currents remain positive in Figures 10e, 10f, 10i, and 10j

and become small or negative in Figures 10g, 10h, 10k, and 10l, in line with expectations from Figure 1i. Figures 10m–10p (fourth row) show the cases where both PPO systems are simultaneously present, either in phase with similar effects being evident or antiphase. These figures again demonstrate dual PPO modulation of the southern currents, as in Figure 8.

3.4. Northern and Southern Separated Subcorotation and PPO-Related Current Profiles
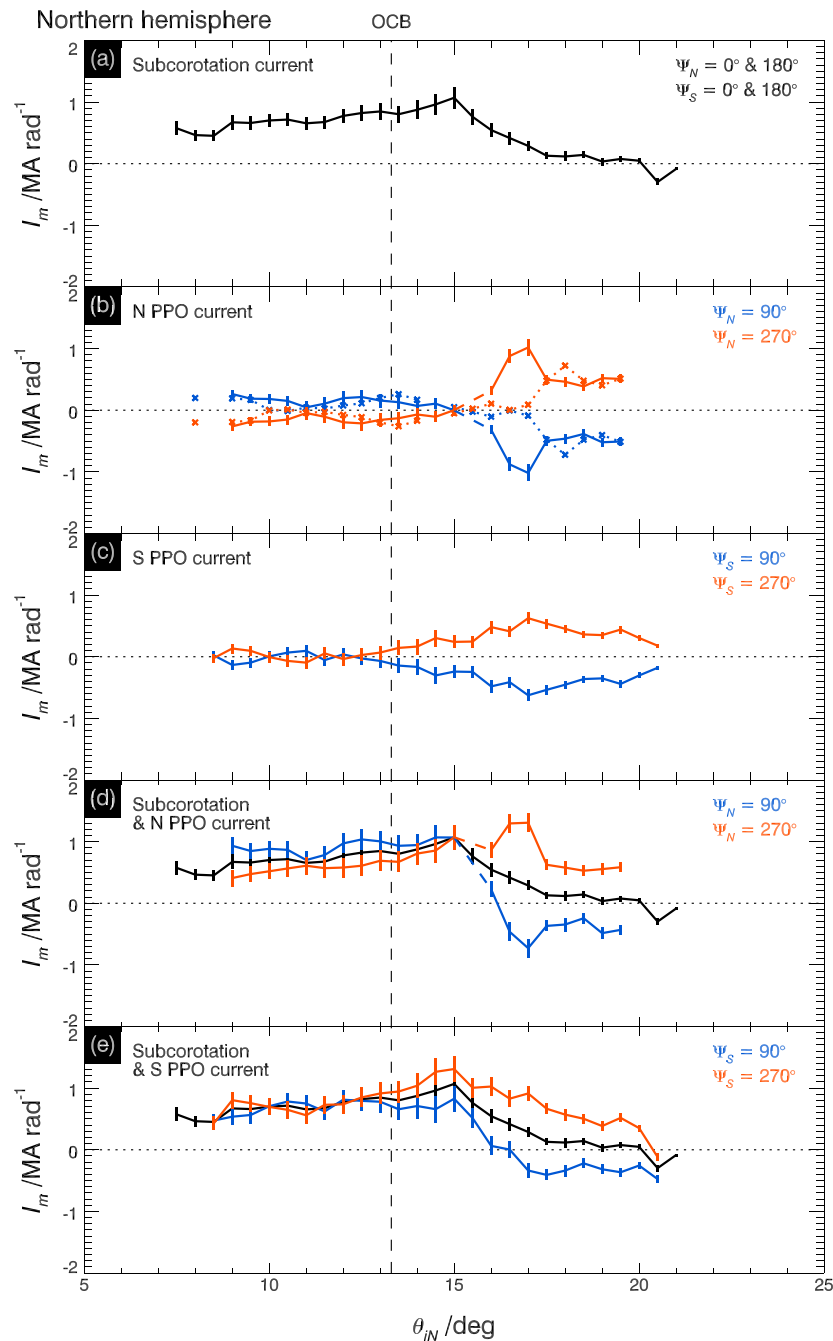### 3.4.1. Subcorotation Current Profiles

The data in Figures 9 and 10 can be used to estimate separated colatitude profiles of the subcorotation and PPO-related currents in the northern and southern hemispheres. Subcorotation currents may first be estimated by combining data from the phase squares for which the PPO effects should be small and average near to zero, that is, Figures 9a–9d and 10a–10d for the northern and southern hemispheres, respectively. Profiles of mean values for the northern and southern data are shown in Figures 11a and 12a, respectively, together with uncertainty estimates given by the standard error of the means. These were computed in the same manner as for Figure 7, with mean values being shown provided at least three Revs contribute to a bin. As may be expected, these profiles are similar to the overall mean profiles in Figures 7b and 7d, respectively. In the northern (summer) hemisphere in Figure 11a a broadly distributed downward current totaling ~6.0 MA (assuming axisymmetry) flows in the polar region to ~15° northern colatitude, ~1.5° equatorward of the OCB, which returns up the field lines between ~15° and ~17.5° centered near the auroral oval (Figure 4e). In the southern (winter) hemisphere in Figure 12a a similar total current flows downward in a narrower polar ring between ~11° and ~15.5° near the OCB, which largely returns up the field lines between ~17° and ~20°. Further discussion is given in sections 3.6 and 3.8.

3.4.2. PPO Current Profiles

An estimate of the northern PPO current profile in the northern ionosphere can also be obtained by combining the data in Figures 9e and 9f, for which $\Psi_N = 90°$ with $\Psi_S = 0°$ and 180°, and separately the data in Figures 9g and 9h, for which $\Psi_N = 270°$ with $\Psi_S = 0°$ and 180°, then subtracting these combined profiles and dividing by two, thus eliminating the common northern subcorotation current. The mean profiles and uncertainties in each case were again derived as for Figure 7, with mean values being retained provided there were at least three contributing Revs. Specifically, the $\Psi_N = 270°$ profile is subtracted from the $\Psi_N = 90°$ profile to obtain the northern PPO profile for $\Psi_N = 90°$ shown by the blue dotted line in Figure 11b and vice versa to obtain the equal but opposite profile for $\Psi_N = 270°$ shown by the red dotted line in Figure 11b. Similarly, the southern PPO current profile in the southern ionosphere can be obtained by combining the data in Figures 10i and 10j for which $\Psi_S = 90°$ with $\Psi_N = 0°$ and 180°, and the data in Figures 10k and 10l for which $\Psi_S = 270°$ with $\Psi_N = 0°$ and 180°, and subtracting and dividing by 2 to yield the red and blue dotted line profiles in Figure 12c. Both northern and southern hemisphere PPO profiles indicate modest near-uniform currents ~0.2 MA rad^{-1} at polar latitudes, which reverse in sense to peak ~4°–5° equatorward of the OCB at ~1 MA rad^{-1} and then modestly decline at larger colatitudes. However, in both cases the profiles show unexpected intervals of near-zero current, equatorward of the OCB for the northern PPO profile in Figure 11b and poleward of the OCB for the southern profile Figure 12c, the possible origin of which is discussed below.

The southern PPO current in the northern ionosphere can be estimated by combining the data in Figures 9i and 9j for which $\Psi_S = 90°$ with $\Psi_N = 0°$ and 180°, also combining the data from Figures 9k and 9l for which $\Psi_S = 270°$ with $\Psi_N = 0°$ and 180°, and subtracting and dividing by 2, with results shown by the blue ($\Psi_S = 90°$) and red ($\Psi_S = 270°$) lines in Figure 11c. Similarly, the northern PPO current in the southern ionosphere can be estimated by combining the data from Figures 10e and 10f for $\Psi_S = 90°$ with $\Psi_S = 0°$ and 180°, also combining the data from Figures 10g and 10h for $\Psi_N = 270°$ with $\Psi_S = 0°$ and 180°, and subtracting and dividing by two, with results shown by the blue ($\Psi_N = 90°$) and red ($\Psi_N = 270°$) lines in Figure 12b. The resulting profiles in both cases show variable near-zero currents in the polar regions, rising to peak ~3°–4° equatorward of the OCB at ~0.6–0.7 MA rad^{-1}, before decreasing more slowly again at larger colatitudes.

We briefly note that the data in Figures 9e–9l and 10e–10l can also be employed to generate additional independent estimates of the subcorotation currents, if instead of subtracting the combined profiles for opposite PPO phases they are added and divided by 2, such that the expected oppositely signed PPO effects then near cancel. Examination shows that these estimates are indeed very similar to those in Figures 11a and 12a, though with larger uncertainties, such that they are not shown here.

Figure 11. Northern hemisphere profiles of the subcorotation and PPO components of the meridional current per radian of azimuth I_m (MA rad^{-1}) derived from the data in Figure 9 are shown plotted versus northern ionospheric colatitude θ_{iN} (deg). (a) The subcorotation (PPO-independent) current derived by combining the data in Figures 9a–9d and deriving mean values in overlapping 1° colatitude bins every 0.5° in the same manner as Figure 7. Uncertainties are estimated as the standard error of the mean. (b) The current associated with the northern PPO system in the northern ionosphere, obtained by subtracting the combined and averaged data for $\Psi_N = 90°$ in Figures 9e and 9f from the combined and averaged data for $\Psi_N = 270°$ in Figures 9g and 9h and dividing by two. Blue and red lines correspond to the equal and opposite profiles for $\Psi_N = 90°$ and 270°, respectively. The crosses joined by dotted lines show the profiles obtained directly from the data in Figures 9e–9h. The solid lines show the profiles obtained after shifting the $\Psi_N = 90°$ data by 1° poleward and the $\Psi_N = 270°$ data by 1° equatorward before subtraction, as described in the text. Uncertainties are estimated from the standard errors of the means of the two subtracted profiles. Values are shown only for colatitude bins in which at least three Revs contribute to each of the subtracted profiles, with dashed line interpolation being shown between. (c) The current of the southern PPO system in the northern ionosphere, obtained by subtracting the combined and averaged data for $\Psi_S = 90°$ in Figures 9i and 9j from the combined and averaged data for $\Psi_S = 270°$ in Figures 9k and 9l and dividing by two. Blue and red lines correspond to the equal and opposite profiles for $\Psi_S = 90°$ and 270°, respectively. Uncertainties are estimated as for Figure 11b. (d) The subcorotation and northern (corrected) PPO currents combined, with uncertainties obtained from the individual profiles and (e) the subcorotation and southern PPO currents combined. The vertical black dashed line shows the averaged position of the OCB in the northern hemisphere (Jinks et al., 2014).
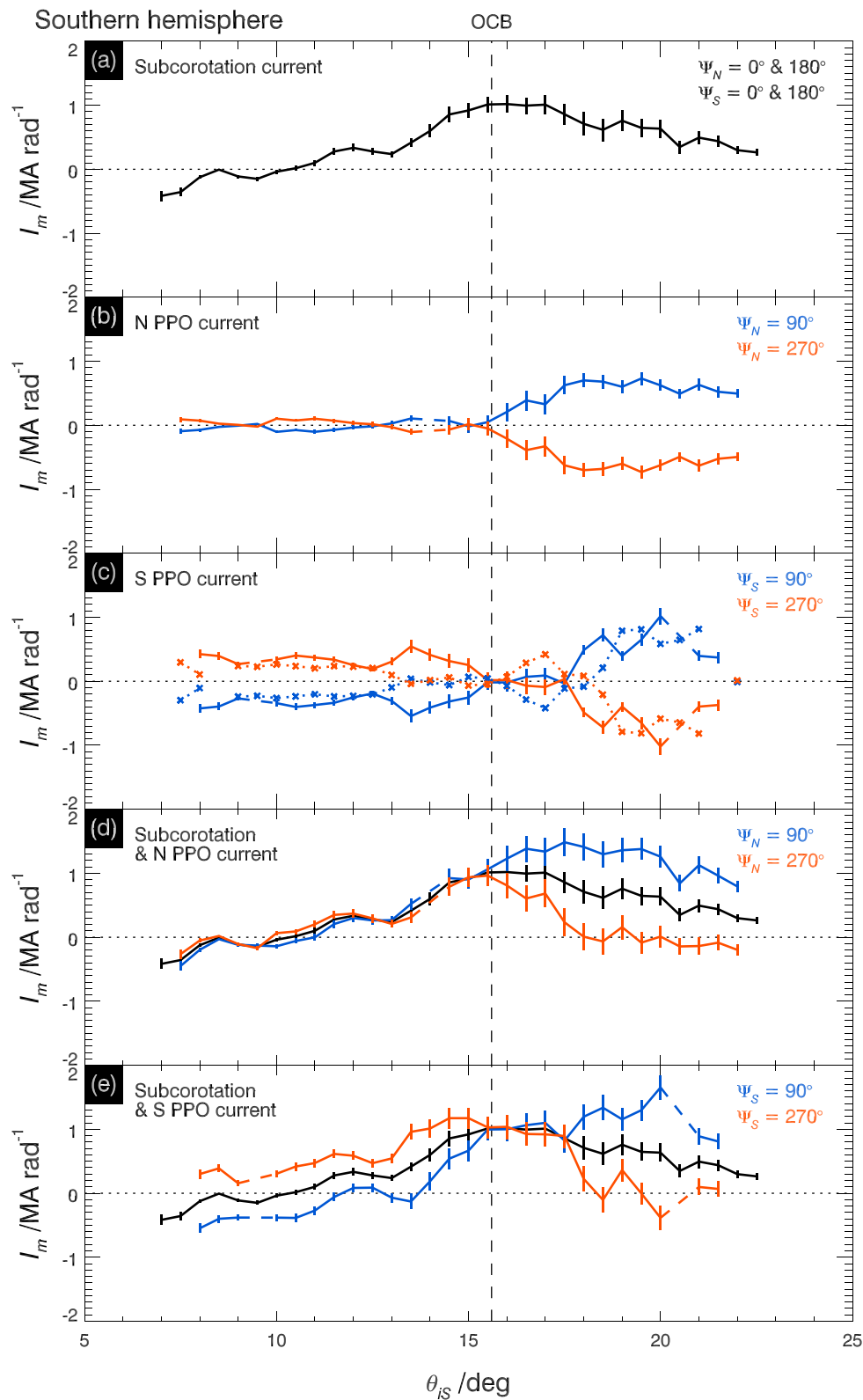
Figure 12. (a–e) Southern hemisphere profiles of the subcorotation and PPO components of the meridional current per radian of azimuth I_m (MA rad^{-1}) derived from the data in Figure 10 are shown plotted versus southern ionospheric colatitude θ_{iS} (deg). The format is the same as Figure 11, except that in this case latitude shifts have been applied to the profiles contributing to Figure 12c, where the solid lines have been derived by shifting the data for $\Psi_S = 90°$ in Figures 10i and 10j by 1° equatorward and the data for $\Psi_S = 270°$ in Figures 10k and 10l by 1° poleward prior to subtraction. The vertical black dashed line shows the averaged position of the OCB in the northern hemisphere (Jinks et al., 2014).

3.4.3. Correction of PPO Current Profiles for the Effects of Latitudinal Oscillation

The results in Figures 11b (dotted lines) and 12b for the northern PPO currents in the northern and southern ionospheres, respectively, and 12c (dotted lines) and 11c for the southern PPO current in the two hemispheres, both appear to suggest rather different current profiles in the two hemispheres. For the northern PPO system, for example, the current profile deduced in the northern hemisphere has near-zero values within several degrees of the OCB, while in the southern hemisphere the current grows gradually away from the OCB. Similarly, the southern PPO current deduced in the southern hemisphere reverses sense ~2.5° equatorward of the OCB, while the southern PPO current in the northern hemisphere again grows gradually away from the OCB. A possible contributor to these differences lies in an effect observed in the well-characterized 2008 southern hemisphere data set investigated by Hunt et al. (2014), for which dual modulation was not significant. This study revealed that the current layers in the southern hemisphere oscillated in latitude near sinusoidally, being displaced by ~1° poleward near $\Psi_S \approx 90°$ and ~1° equatorward near $\Psi_S \approx 270°$, an effect attributed to the action of the rotating twin-vortex flow in the southern hemisphere shown by the red dashed lines in Figure 1g. Such an effect is far more difficult to observe directly in the data employed here for reasons discussed in section 2. Given the expected flows in the northern ionosphere shown by the red dashed lines in Figure 1d, the anticipated equivalent effect in the northern hemisphere is a comparable equatorward displacement of the current layers at $\Psi_N \approx 90°$ and a poleward displacement at $\Psi_N \approx 270°$.

If we consider the effect of such shifts on the differenced profiles employed to estimate the northern PPO current in the northern ionosphere (dotted lines in Figure 11b) and the southern PPO profile in the southern hemisphere (dotted lines in Figure 12c), it is readily seen that the effect on the oppositely signed PPO currents themselves is small, serving only to modestly broaden the current profile. However, similar shifts of the subcorotation current profile, followed by subtraction and division by 2, result in spurious contributions to the PPO-dependent current profiles. Specifically, in the northern hemisphere it leads for a phase of $\Psi_N \approx 90°$ to the addition of a negative current in the poleward region where the subcorotation current increases with colatitude and a positive current in the equatorward region where the subcorotation current decreases with colatitude, with equal and opposite effects for $\Psi_N \approx 270°$. In the southern hemisphere the senses of these effects are reversed. Addition of such spurious differences to the expected PPO currents then reduces the expected PPO-related currents in both hemispheres, thus potentially explaining the suppression of the PPO currents in Figures 11b and 12c, particularly in those colatitude intervals where the subcorotation current varies strongly with colatitude (see Figures 11a and 12a). This effect does not apply to the southern PPO profile in the northern ionosphere (Figure 11c), however, nor the northern PPO profile in the southern ionosphere (Figure 12b), since these were determined for $\Psi_N = 0°$ and 180° in the northern hemisphere and for $\Psi_S = 0°$ and 180° in the southern hemisphere, for which the displacements are expected to be near zero. This assumes, of course, that the northern PPO system flow driven in the southern ionosphere along field lines from the north, and vice versa, are secondary effects.

To investigate these effects, we have appropriately shifted the profiles in colatitude by 1° to bring them into alignment for $\Psi_{N,S} = 90°$ and 270° before subtraction and division by two. Specifically, in the northern hemisphere we have shifted the combined $\Psi_N = 90°$ profile poleward by 1° and the combined $\Psi_{N,S} = 270°$ profile equatorward by 1° before subtraction, while in the southern hemisphere we have shifted the combined $\Psi_S = 90°$ profile equatorward by 1° and the combined $\Psi_S = 270°$ profile poleward by 1° before subtraction. The modified corrected current profiles are shown by the solid blue and red lines in Figures 11b and 12c. In the northern hemisphere the overall profiles now reverse sign directly from small polar values to much larger auroral region values ~2° equatorward of the OCB. Similarly in the southern hemisphere, the unexpected interval of weak polar values just poleward of the OCB is removed, the polar currents now being essentially continuous, while weaker currents occur in the reversal region ~2° equatorward of the OCB. Overall, these corrected profiles are in better agreement with each other and with expectation, and will hence be adopted here in further discussion.

3.4.4. Subcorotation and Individual PPO System Current Profiles

Figure 11d shows our estimate of the overall northern hemisphere profile at the peaks of the northern PPO current but in the absence of the southern PPO current, while Figure 11e correspondingly shows the overall northern hemisphere profile at the peaks of the southern PPO current in the absence of the northern PPO current. That is, Figure 11d corresponds to $\Psi_N = 90°$ (blue) and $\Psi_N = 270°$ (red) with $\Psi_S = 0°$ and 180°,

derived by combining the profile for the subcorotation current in Figure 11a, reproduced in black in Figures 11d and 11e, with the corresponding corrected profiles for the PPO-related currents in Figures 11b and 11c. In Figure 11d we note that the addition of the northern PPO current nearly doubles the upward directed current in the auroral region when $\Psi_N = 90°$, while considerably reducing it over the colatitude range shown when $\Psi_N = 270°$. Figure 11e shows that the southern PPO currents in the northern hemisphere have a similar effect but of lesser magnitude. Figures 12d and 12e show corresponding results in the southern hemisphere for the overall current at the peaks of the northern PPO current in the absence of the southern PPO current and at the peaks of the southern PPO current in the absence of the northern PPO current, respectively. Again, major modulations of the current profiles equatorward of the OCB are observed, with stronger upward currents for $\Psi_{N,S} = 270°$ and weaker for $\Psi_N = 90°$.

We finally recall that due to the finite width of the phase square bins the PPO-related profiles in Figures 11 and 12 will generally represent values slightly smaller than those at the extrema at $\Psi_{N,S} = 90°$ and 270°. If the variations are near sinusoidal in PPO phase, however, the expected factor is only $2\sqrt{2}/\pi \approx 0.90$, as mentioned in section 3.3. The PPO values in these figures can be multiplied by $\pi/2\sqrt{2} \approx 1.11$ for a better estimate of the true peak if required.

3.5. Comparison of Model Current Profiles With Dual-Modulated Data
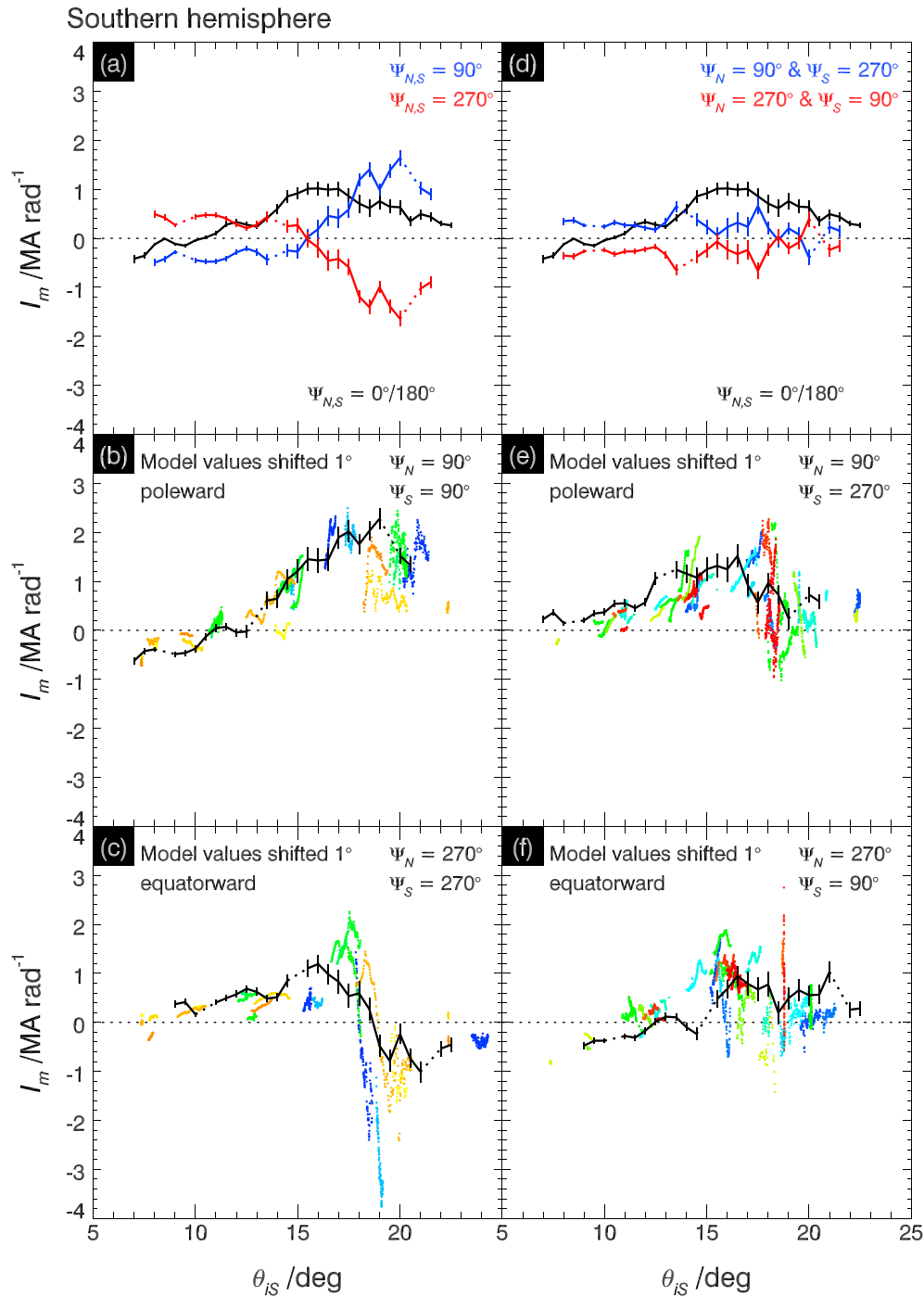
The derivation of the northern and southern hemisphere current profiles in Figures 11 and 12 employed data from 12 out of the total of 16 phase squares in Figures 9 and 10. The subcorotation profiles were derived using the phase squares for which neither northern nor southern PPO system should on average be present, while the individual PPO-related profiles were derived from those in which one system should be present, but not the other. The data from the remaining 4 phase squares for each hemisphere that are expected to be dual modulated by both PPO systems (Figures 9m–9p and 10m–10p), either in phase or antiphase with each other, were not employed in the derivation of Figures 11 and 12, thus providing the opportunity for an independent check on the results. That is, to say, we can synthesize northern and southern hemisphere model current profiles corresponding to in-phase and antiphase dual-modulated PPO conditions from the results in Figures 11a–11c and 12a–12c and compare them with the independent northern and southern hemisphere data in Figures 9m–9p and 10m–10p.

Results are shown for the northern hemisphere in Figure 13, for in-phase PPO conditions in Figures 13a–13c and antiphase in Figures 13d–13f. Figure 13a shows the combined PPO-related current profiles for the cases where Ψ_N and Ψ_S are both 90° (blue) and both 270° (red), obtained from Figure 11b (corrected) profiles and 11c, together with the subcorotation current profile from Figure 11a (black). Figure 13b shows the combined subcorotation plus PPO current profiles with Ψ_N and Ψ_S both 90°, together with the color-coded data from Figure 9m, while Figure 13c shows the combined subcorotation plus PPO current profiles for Ψ_N and Ψ_S both 270°, together with the data from Figure 9n. In accordance with the discussion in section 3.4.3 the former profile has also been shifted 1° equatorward and the latter 1° poleward, though this does not strongly affect the comparison. Despite the data scatter, the overall agreement is seen to be reasonable, with slowly increasing positive polar values decreasing to negative auroral region values in Figure 13b, while smaller positive polar values increase to larger values in the auroral region before falling again in Figure 13c. Figure 13d similarly shows the combined PPO current profiles when the two systems are in antiphase, for the cases where $\Psi_N = 90°$ and $\Psi_S = 270°$ (blue line) and $\Psi_N = 270°$ and $\Psi_S = 90°$ (red line), again obtained from Figures 11b (corrected profile) and 11c, together with the subcorotation current from Figure 11a (black line). Figure 11e then shows the overall current profile corresponding to antiphase conditions $\Psi_N = 90°$ and $\Psi_S = 270°$ (again shifted 1° equatorward) together with the color-coded data from Figure 9o, while Figure 11f shows the overall profile for the opposite antiphase condition $\Psi_N = 270°$ and $\Psi_S = 90°$ (again shifted 1° poleward) together with the data from Figure 9p. The overall agreement is again seen to be reasonable, with a sharp switch from larger positive polar to near-zero values in Figure 11e and smaller currents with similar behavior occurring in Figure 11f.

Figure 14 shows results for the southern hemisphere currents, derived from combinations of subcorotation and PPO-related current profiles shown in Figure 12 (the corrected profiles in Figure 12c), again shifted by 1° poleward for $\Psi_S = 90°$ and 1° equatorward for $\Psi_S = 270°$, together with the color-coded data from Figures 10m–10p. Reasonable overall agreement is again noted, with a large near-monotonic increase in
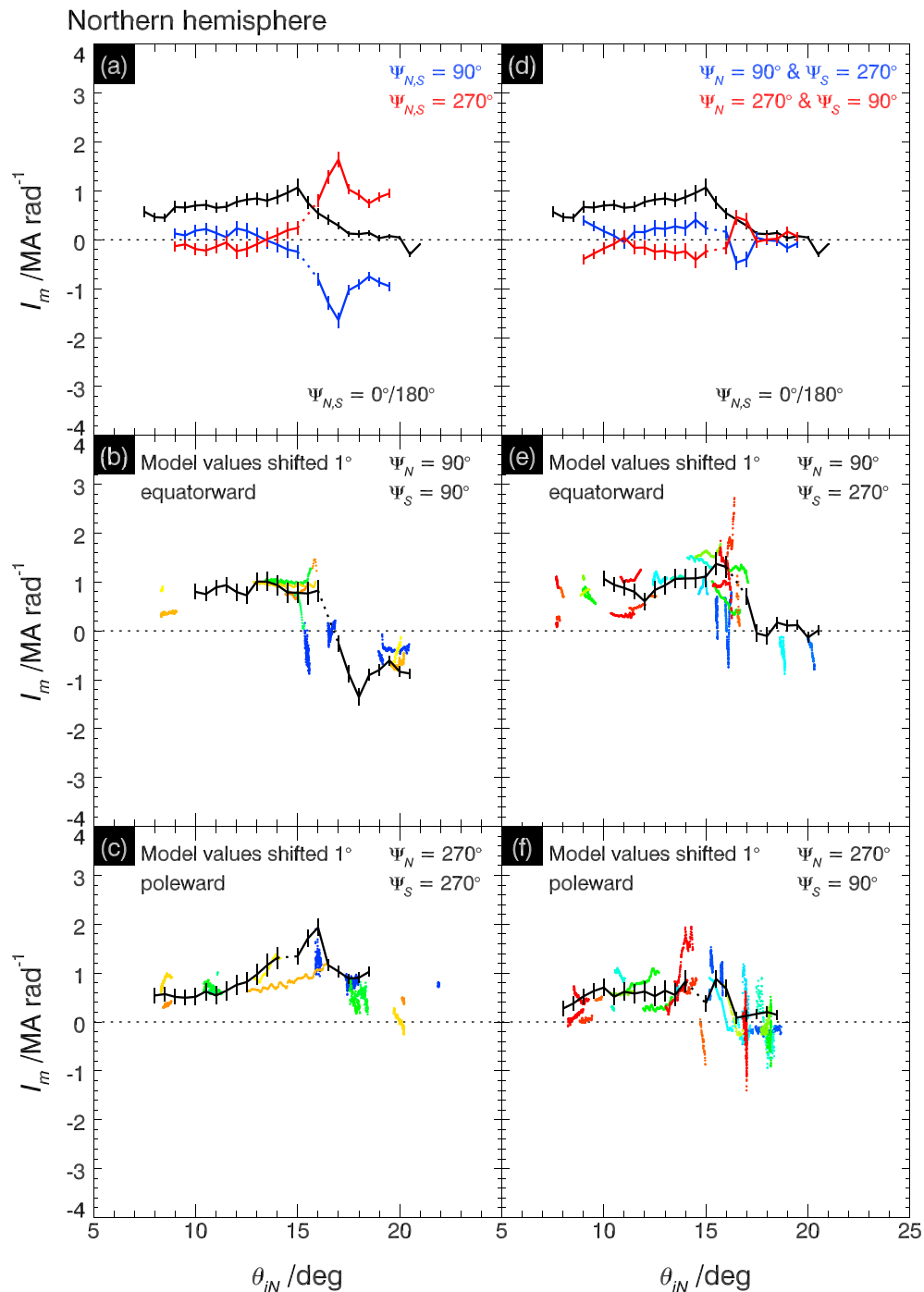
Figure 13. Comparison of northern hemisphere model profiles of the meridional current per radian of azimuth I_m (MA rad^{-1}) derived from results in Figure 11 for cases of dual modulation by both northern and southern PPO systems, and the corresponding independent data shown in Figures 9m–9p. Cases for which the two PPO systems are in phase, $\Psi_{N,S} = 90°$ and $270°$, are shown in Figures 13a–13c, while cases for which the two systems are in antiphase, $\Psi_N = 90°$ with $\Psi_S = 270°$ and $\Psi_N = 270°$ with $\Psi_S = 90°$ are shown in Figures 13d–13f. (a) The subcorotation profile (black) from Figure 11a together with the equal and opposite combined northern and southern PPO profiles for $\Psi_{N,S} = 90°$ (blue) and $270°$ (red) from Figure 11b (solid line corrected profiles) and Figure 11c. (b) The subcorotation and $\Psi_{N,S} = 90°$ profiles are added, shifted by 1° equatorward (for $\Psi_N = 90°$), and compared with the color-coded data in Figure 9m. (c) The subcorotation and $\Psi_{N,S} = 270°$ profiles are added, shifted by 1° poleward (for $\Psi_{N,S} = 270°$), and compared with the data in Figure 9n. (d) The subcorotation profile (black) from Figure 11a together with the equal and opposite combined northern and southern PPO profiles for $\Psi_N = 90°$ with $\Psi_S = 270°$ (blue) and $\Psi_N = 270°$ with $\Psi_S = 90°$ (red) from Figure 11b (solid line corrected profiles) and Figure 11c. (e) The subcorotation and $\Psi_N = 90°$ with $\Psi_S = 270°$ profiles are added, shifted by 1° equatorward (for $\Psi_N = 90°$), and compared with the data in Figure 9o. (f) The subcorotation and $\Psi_N = 270°$ with $\Psi_S = 90°$ profiles are added, shifted by 1° poleward (for $\Psi_N = 270°$), and compared with the data in Figure 9p.

Figure 14. Comparison of southern hemisphere model profiles of meridional current per radian of azimuth I_m (MA rad^{-1}) derived from the results in Figure 12 for cases of dual modulation by both northern and southern PPO systems, with the corresponding independent data shown in Figures 10m–10p. The cases for which the two systems are in phase, $\Psi_{N,S} = 90°$ and $270°$, are shown in Figures 14a–14c, while the cases for which the two systems are in antiphase, $\Psi_N = 90°$ with $\Psi_S = 270°$ and $\Psi_N = 270°$ with $\Psi_S = 90°$ are shown in Figures 14d–14f. The format is the same as for Figure 13.

current with colatitude to ~18°–19° occurring for $\Psi_{N,S} = 270°$ in Figure 14b and a large switch from positive to negative values with increasing colatitude for $\Psi_{N,S} = 270°$ in Figure 14c, though the latter is considerably smoothed in the model profiles deduced from Figure 12. Overall, however, the comparisons shown in Figures 13 and 14 lend confidence to our results in Figures 11 and 12 and the methodology employed to generate them.

3.6. Comparison of Current Profiles in the Northern and Southern Hemispheres

Figure 15 compares the subcorotation and PPO-related current profiles in the two hemispheres. The northern hemisphere currents are shown by solid lines plotted versus northern ionospheric colatitude, while to allow detailed comparison the southern hemisphere currents have been mapped to the northern ionosphere to points of equal enclosed polar magnetic flux (equivalent to "along field lines" in the closed field region) and are shown by crosses and dotted lines. An equivalent (slightly nonlinear) scale of southern ionospheric colatitude is shown at the top of the figure. To avoid clutter, uncertainty values are shown only for the northern profiles, noting that the uncertainties for the southern profiles are entirely comparable (Figures 11 and 12). Vertical dashed lines show the northern (blue) and mapped southern (red) OCBs estimated by Jinks et al. (2014). In principle, these two boundaries must map to the same position as each other, enclosing the same amount of polar open flux, so that the difference seen in the figure represents a measure of their uncertainty.
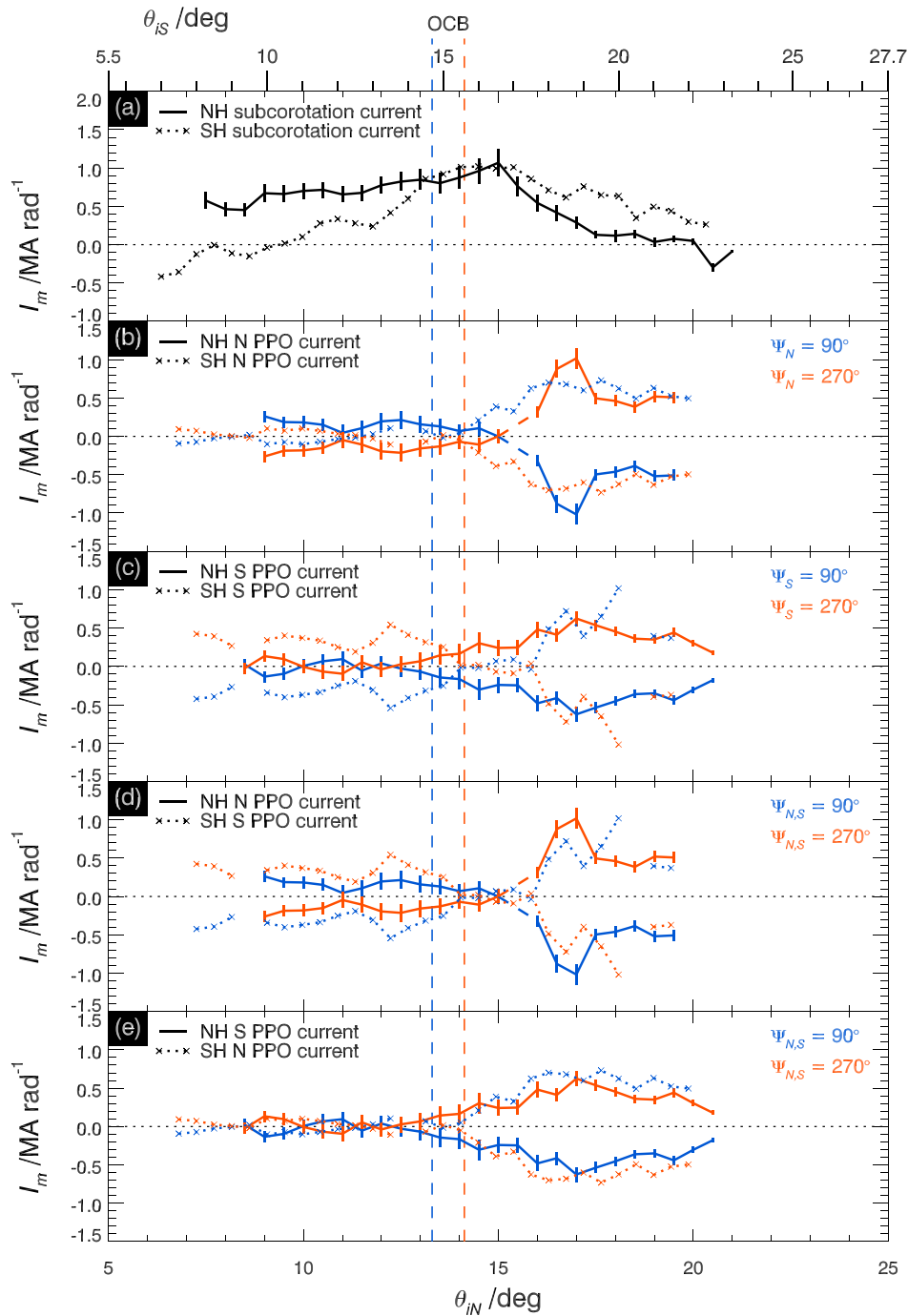
Figure 15a compares the northern and southern hemisphere subcorotation current profiles, whose form follows the previous discussion in section 3.1 (Figures 7b and 7d) and section 3.4 (Figures 11a and 12a). Here we see that the current values in the two hemispheres reach closely similar ~1 MA rad^{-1} peak values on the same field lines in the vicinity of the OCB and just equatorward thereof but deviate from each other in opposite senses on either side of the boundary. In the southern polar region the current falls rapidly to small values ~3°–4° poleward of the OCB while in the northern polar region the current falls much more gradually. In the equatorward region the current in the northern hemisphere falls rapidly to small values ~2.5° equatorward of the peak, while in the southern hemisphere the current falls more gradually in this region.

Figure 15b compares the northern PPO current in the "driving" northern hemisphere (solid lines) with the northern PPO current in the "responding" southern hemisphere (dotted lines). Similarly, Figure 15c compares the southern PPO current in the driving southern hemisphere (dotted lines) with the southern PPO current in the responding northern hemisphere (solid lines). In both cases, the near-constant polar values at smallest colatitudes in the driving hemispheres reverse sense across a fairly broad region equatorward of the OCB before peaking at ~1 MA rad^{-1} in both hemispheres at larger colatitudes, and then falling again. Also in both cases, the current in the responding hemispheres increases more gradually with colatitude from near-zero values at and poleward of the OCB to peak at ~0.7 MA rad^{-1} for the northern PPO system and ~0.6 MA rad^{-1} for the southern PPO system and then fall again to values similar to those in the driving hemispheres. The difference between the driving and responding currents for a given system relates to the cross-field magnetospheric closure currents illustrated in Figures 1f and 1i, as will be discussed in section 3.7.

Figures 15d and 15e compare the driving and responding current profiles in the two hemispheres, respectively. Overall, the two systems have near-equal amplitudes in agreement with expectation from Figure 3c. The unexpected differences in detailed form between the driving and responding current profiles (see Figures 1f and 1i) may arise from averaging over a number of Revs with varying OCB positions, in the presence of a current reversal in the polar region in the case of the driving currents, but with near-zero current in the polar region in the case of the responding current.

3.7. Overall Current Continuity in the PPO Systems

We now give a brief discussion of current closure in the two PPO systems based on the results in Figure 15 and first consider continuity in the northern PPO system as indicated in Figure 15b. An overall schematic is provided in Figure 16a where the arrowed black lines show cross-field currents in both the ionosphere (short dashed circle) and magnetosphere, blue areas and arrows field-aligned currents flowing from the northern ionosphere to the southern, and red areas and arrows field-aligned currents flowing from the southern ionosphere to the northern. Arrows are labeled with the corresponding current in MA rad^{-1} as indicated below, referring specifically to peak values on the $\Psi_N = 90° - 270°$ meridian (Figure 1e). From Figure 15b it is seen that the main northern PPO field-aligned current in the northern hemisphere, flowing in a ~3° colatitude band from just equatorward of the OCB to ~17° (mapping to ~11 R_S in the equatorial plane) totals ~1.2 MA rad^{-1}, directed upward at $\Psi_N = 90°$ and downward at $\Psi_N = 270°$ as indicated in Figure 16a. The contributions to this total current are ~0.2 MA rad^{-1} from the polar ionosphere and ~1.0 MA rad^{-1} from closed field lines at larger colatitudes. Of the total field-aligned current, ~0.7 MA rad^{-1}, that is, somewhat over half, flows on these field lines into the southern ionosphere, downward at $\Psi_N = 90°$ and upward at $\Psi_N = 270°$ as

Figure 15. Comparison of meridional current per radian of azimuth I_m (MA rad^{-1}) colatitude profiles for the northern and southern hemispheres shown in Figures 11 and 12, respectively. Southern current profiles (crosses and dotted lines) from Figures 12a–12c have been mapped to the northern ionosphere to points of equal enclosed polar magnetic flux (along field lines in the closed field region) and plotted versus northern colatitude together with the northern current profiles from Figures 11a–11c (solid lines). An equivalent southern colatitude scale is shown at the top of the figure. Vertical dashed lines show the colatitudes of the northern (blue) and mapped southern (red) OCBs according to Jinks et al. (2014), the difference between them giving a measure of their uncertainty. For the PPO current profiles, those for $\Psi_{N,S} = 90°$ are shown blue, while the equal and opposite profiles for $\Psi_{N,S} = 270°$ are shown red. For clarity, standard error of the mean uncertainty estimates are shown only for the northern profiles, the comparable uncertainties for the southern profiles are shown in Figure 12. (a) Comparison between northern and southern hemisphere subcorotation (PPO-independent) current profiles (Figures 11a and 12a). (b) Comparison between northern and southern hemisphere northern PPO system current profiles (Figures 11b and 12b). (c) Comparison between northern and southern hemisphere southern PPO system current profiles (Figures 11c and 12c). (d) Comparison between the northern hemisphere northern PPO current profile with the southern hemisphere southern PPO current profile (Figures 11b and 12c). (e) Comparison between the northern hemisphere southern PPO current profile with the southern hemisphere northern PPO current profile (Figures 11c and 12b). NH = northern hemisphere; SH = southern hemisphere.
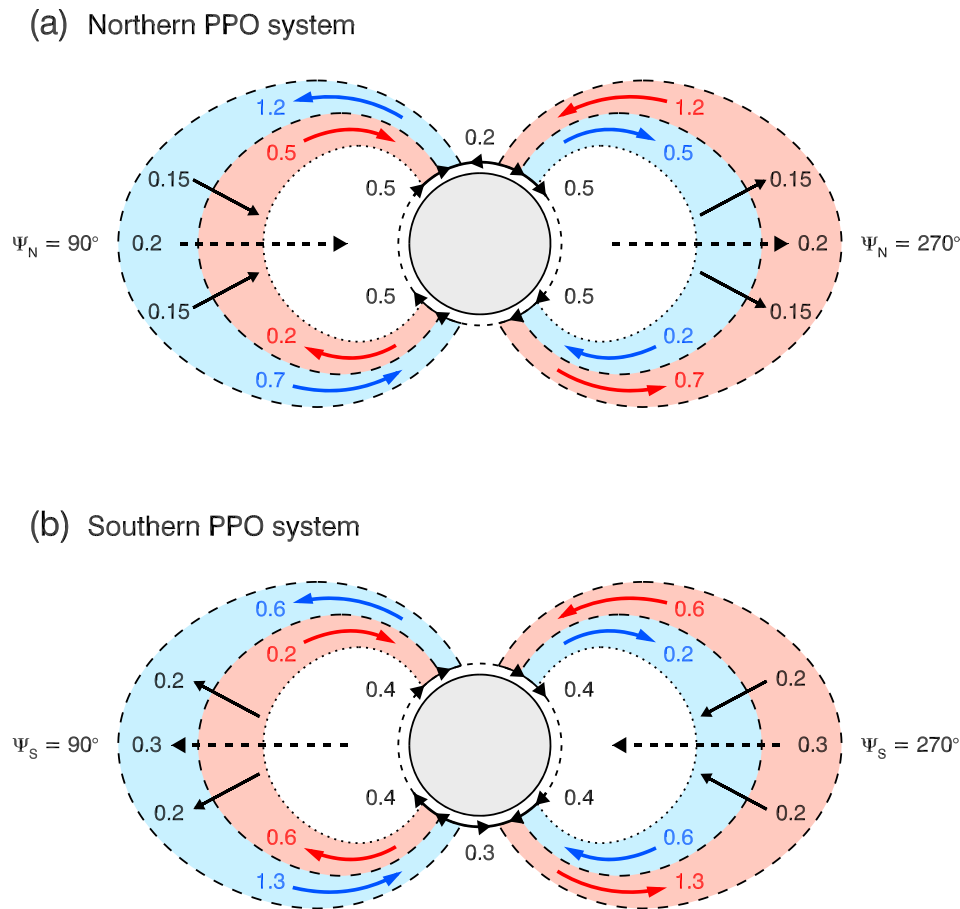
Figure 16. Sketches illustrating the overall current flow in the two PPO systems based on the results in Figures 15b and 15c. The arrowed black lines show cross-field currents in both the ionosphere (short dashed circle) and magnetosphere, blue areas and arrows field-aligned current flows from the northern ionosphere to the southern, and red areas and arrows field-aligned current flows from the southern ionosphere to the northern. Arrows are labeled with the corresponding current in MA rad^{-1}, referring specifically to maximum values on the $\Psi_N = 90° − 270°$ meridian for the northern system in Figure 16a (see Figure 1e), and on the $\Psi_S = 90° − 270°$ meridian for the southern system in Figure 16b (see Figure 1h), though the values given may be multiplied by a factor of ~1.1 to account for averaging the data over phase squares. The numbers may also be converted to total azimuth-integrated currents of a given sense flowing either side of the planet by multiplying by a factor of ~2.2 (section 3.7). The equatorial long dashed black arrows either side of the planet indicate the total cross-field current flowing in the magnetosphere between the two meridians into and out of the plane of the sketch, equal to the ionospheric transpolar current flow. The inner dotted field lines indicate the boundary of the region accessible to the data employed in this study.

shown in the figure. The difference between these currents indicates that ~0.5 MA rad^{-1} closes cross field in the magnetosphere in the region between. No significant additional contribution to the northern system current comes from the southern polar ionosphere. Equatorward of this main current layer, between ~17° and ~18.5° northern colatitude, corresponding to ~19° and ~20.5° southern colatitude (mapping between ~11 and ~8 R_S in the equatorial plane), a small reversed "return" field-aligned current of ~0.2 MA rad^{-1} flows in the southern ionosphere, upward at $\Psi_N = 90°$, and downward at $\Psi_N = 270°$, while on the same field lines in the northern ionosphere a larger return field-aligned current of ~0.5 MA rad^{-1} flows, downward at $\Psi_N = 90°$ and upward at $\Psi_N = 270°$. This difference indicates that of the total ~0.5 MA rad^{-1} cross-field closure current estimated above, ~0.3 MA rad^{-1} closes via return currents to the northern ionosphere (Figure 1e), shown for convenience of drawing as two contributions (black arrows) of 0.15 MA rad^{-1} either side of the equator in Figure 16a. The remaining ~0.2 MA rad^{-1}, equal and opposite to the polar current, closes cross field in the magnetosphere to the opposite magnetic meridian, shown in the figure by the equatorial long dashed black arrows either side of the planet, indicating current flow out of and/or into the plane of the sketch. An ionospheric meridional current of ~0.5 MA rad^{-1} remains flowing in both hemispheres at the large colatitude limit of the data at 20° northern and 22° southern colatitudes (~6.5 R_S in the equatorial plane), indicated by the inner dotted field lines in Figure 16a. These lower-

latitude ionospheric currents are shown by the black arrows in the figure, directed south to north at $\Psi_N = 90°$ and north to south at $\Psi_N = 270°$, whose mode of closure is inaccessible to these data but likely involves further field-aligned current flow interior to the region depicted.

Similarly, for the southern PPO system in Figure 15c, sketched in Figure 16b in a similar format to Figure 16a and showing peak currents per radian on the $\Psi_S = 90° - 270°$ meridian (Figure 1h), the main field-aligned current in the southern hemisphere flowing in a ~5° colatitude band from near the OCB to ~20° southern colatitude (mapping to ~9 R_S in the equatorial plane) totals ~1.3 MA rad^{-1}, flowing downward at $\Psi_S = 90°$ and upward at $\Psi_S = 270°$. The contributions to this total current are ~0.3 MA rad^{-1} from the southern polar ionosphere and ~1.0 MA rad^{-1} from the closed field region at larger colatitudes. Of the total field-aligned current, ~0.6 MA rad^{-1} (i.e., slightly under half) flows into the northern ionosphere, upward at $\Psi_S = 90°$ and downward at $\Psi_S = 270°$, the difference again indicating that ~0.7 MA rad^{-1} closes cross field in the magnetosphere. No significant additional contributions come from the northern polar ionosphere. Equatorward of these main currents, a small reversed return field-aligned current of ~0.2 MA rad^{-1} flows in the northern ionosphere, downward at $\Psi_S = 90°$, and upward at $\Psi_S = 270°$, while on these field lines in the southern ionosphere a larger return field-aligned current of ~0.6 MA rad^{-1} flows, upward at $\Psi_S = 90°$, and downward at $\Psi_S = 270°$. This difference indicates that of the total ~0.7 MA rad^{-1} cross-field closure current mentioned above, ~0.4 MA rad^{-1} closes via these return currents to the southern ionosphere (Figure 1h), again shown as two contributions of 0.2 MA rad^{-1} either side of the equator in Figure 16b, while the remaining ~0.3 MA rad^{-1} (equal and opposite to the polar current) closes cross magnetosphere in the opposite magnetic meridian, again shown by the equatorial long dashed black arrows either side of the planet. An ionospheric meridional current of ~0.4 MA rad^{-1} also remains flowing at the ~21.5° southern colatitude outer limit of joint northern and southern data in both hemispheres, directed south to north at $\Psi_S = 90°$ and north to south at $\Psi_S = 270°$, whose mode of closure is again inaccessible to these data (inner dotted field lines).

Within the limitations of accessibility, these results thus indicate that the PPO-related field-aligned currents close principally in the reversed current layers occurring separately in the $\Psi_{N,S} = 270°$ and 270° meridians, with relatively smaller currents, ~20% of the total, being involved in the transpolar and trans-meridional flow. Of the current flowing in the meridians, roughly half closes cross field within the magnetosphere, and half via the opposite ionosphere (Figures 1e and 1h).

We note that the above discussion (and Figure 15) has been in terms of the maximal PPO-related meridional currents per radian of azimuth on the $\Psi_{N,S} = 90° - 270°$ meridians. However, assuming the currents vary near sinusoidally with PPO phase the values can simply be converted to total currents of a given sense by multiplying by a factor of 2. Account can also be taken of the likely reduction in quoted peak values by a factor of $\left(2\sqrt{2}/\pi\right) \approx 0.90$ resulting from data averaging in 90° × 90° phase squares as described in section 3.3, such that current per radian for the PPO systems can be converted into total current of a given sense by multiplying by a factor of $2/\left(2\sqrt{2}/\pi\right) = \left(\pi/\sqrt{2}\right) \approx 2.2$.

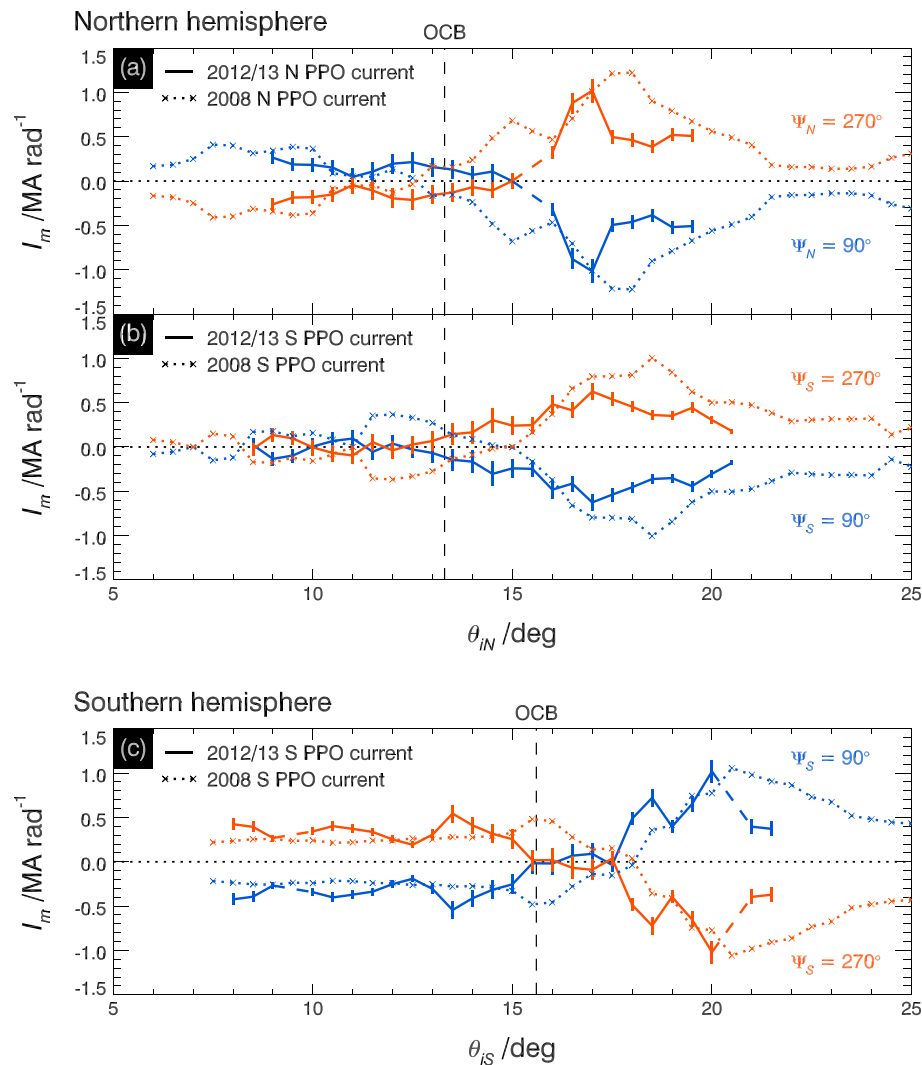### 3.8. Comparison of Results With the 2008 Data Set

We now compare our results with those derived from the 2008 data set, specifically those of Hunt et al. (2014) for the southern hemisphere data and Hunt et al. (2015) for the northern hemisphere data. We recall from Figure 3a that the 2008 data set corresponds to late Saturn southern summer with solar latitudes between −8° and −4°, while the 2012/2013 data analyzed here correspond to midnorthern spring with solar latitudes between +15° and +19°. For simplicity we will refer to the southern hemisphere in 2008 and the northern hemisphere in 2012/2013 as the "summer" hemispheres, and the northern hemisphere in 2008 and the southern hemisphere in 2012/2013 as the "winter" hemispheres.

We begin with the subcorotation currents and in Figure 17 compare the northern and southern current profiles for the 2012/2013 data set (solid lines from Figures 11a and 12a) and those derived by Hunt et al. (2014, 2015) for the 2008 data set (crosses joined by dotted lines). Figures 17a and 17c directly compare the northern and southern hemisphere subcorotation currents, respectively, derived from the 2012/2013 and 2008 data sets. In the 2012/2013 data there is a strong difference between the northern and southern subcorotation current profiles as discussed in section 3.6. The profiles from 2008 are seen to show a very similar asymmetry but reversed between hemispheres. The closeness of the comparison is emphasized in Figures 17b and 17d.
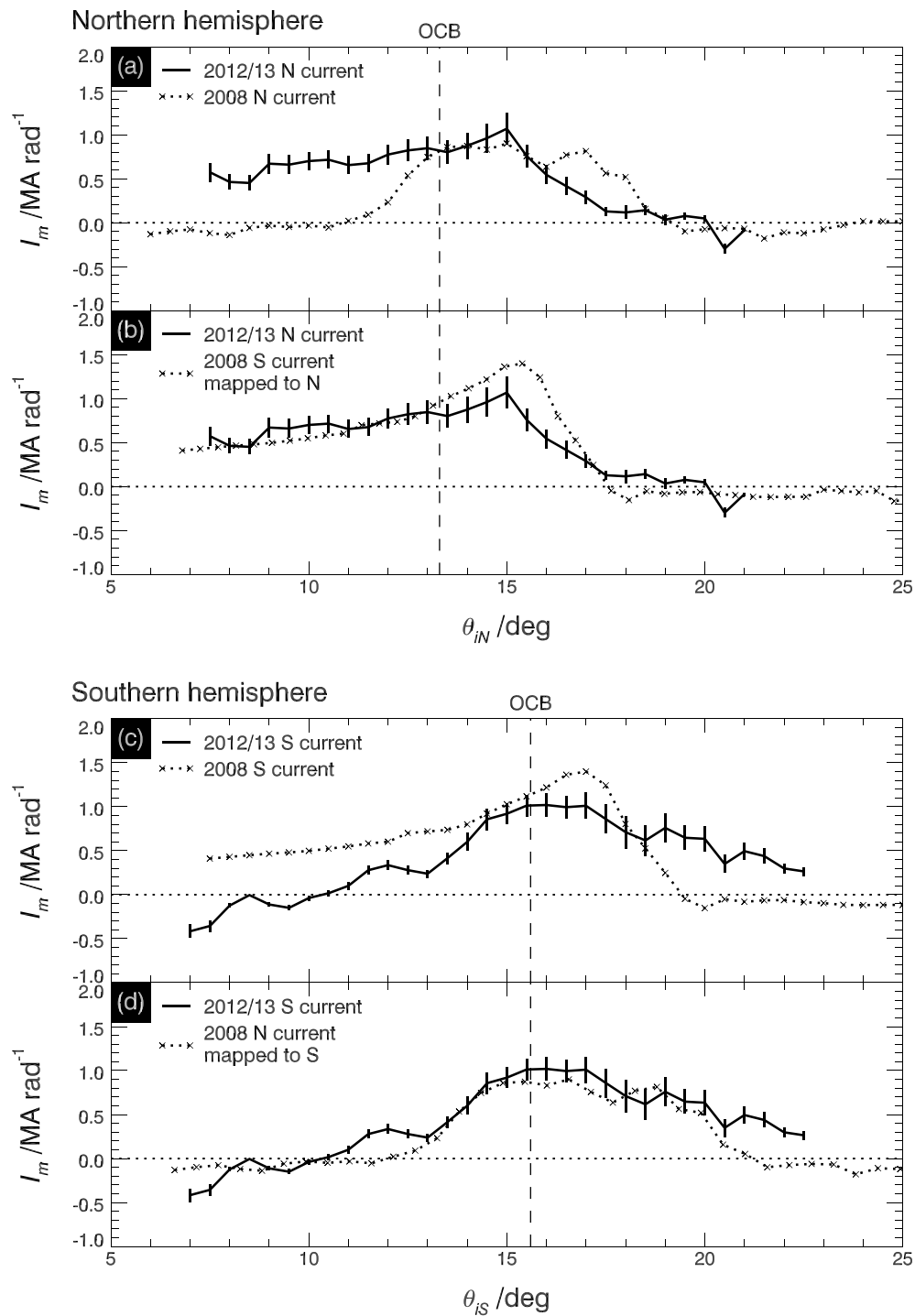
Figure 17. Comparison of the meridional subcorotation (PPO-independent) current I_m (MA rad^{-1}) colatitude profiles derived here from the 2012/2013 data set (solid lines) with those derived by Hunt et al. (2014, 2015) from the 2008 data set (crosses and dotted lines). (a and b) The 2012/2013 northern hemisphere subcorotation current (Figure 11a) plotted versus northern ionospheric colatitude θ_{iN} (deg), compared with the 2008 northern and mapped southern hemisphere subcorotation currents, respectively. (c and d) The 2012/2013 southern hemisphere subcorotation current (Figure 12a) plotted versus southern ionospheric colatitude θ_{iS} (deg), compared with the 2008 southern and mapped northern hemisphere subcorotation currents, respectively. Vertical dashed lines show the averaged position of the OCB for each hemisphere (Jinks et al., 2014).

Figure 17b again shows the northern hemisphere profile from the 2012/2013 data set but now compared with the southern hemisphere profile from 2008 mapped into the northern ionosphere (as in Figure 15). The profiles are seen to be very similar, though the 2008 data peak at slightly larger values at slightly larger colatitudes. In

Figure 18. Comparison of ionospheric PPO-related meridional current profiles derived here from the 2012/2013 data set (solid lines) with corresponding profiles derived by Hunt et al. (2014, 2015) from the 2008 data set (crosses and dotted lines). Profiles for $\Psi_{N,S} = 90°$ are shown blue, while equal and opposite profiles for $\Psi_{N,S} = 270°$ are shown red. (a) Comparison of currents of the northern PPO system in the northern hemisphere (the corrected solid line profiles in Figure 11b) and (b) comparison of the currents of the southern PPO system in the northern hemisphere (Figure 11c), plotted versus northern ionospheric colatitude. (c) Comparison of currents of the southern PPO system in the southern hemisphere (the corrected solid line profiles in Figure 12c), plotted versus southern ionospheric colatitude. No northern PPO perturbations could be discerned in the southern hemisphere in 2008. Vertical dashed lines show the averaged OCB for each hemisphere (Jinks et al., 2014).

Figure 17d we again show the southern hemisphere profile from 2012/2013 but now compare it with the northern hemisphere profile from 2008 mapped into the southern ionosphere. The two profiles are again seen to be very similar, including in the polar region despite the detailed seasonal difference between the two intervals, with the polar ionosphere being in permanent darkness to ~6° colatitude for the 2008 data and to ~14° for the 2012/2013 data. Equatorward of the OCB, the current reduces to smaller values more gradually in the winter hemisphere than in the summer hemisphere in both cases, despite the hemispheric symmetry generally expected on closed field lines. Overall, these findings clearly confirm that the hemispheric asymmetries in the subcorotation currents are related to seasonal conditions at Saturn, as suggested by Hunt et al. (2015).

We now compare the PPO-related current profiles derived from the two data sets, noting from Figure 3e that the PPO amplitudes had likely declined modestly between the two intervals. Comparisons are shown in Figure 18, where again solid lines show the profiles for the 2012/2013 data set (Figures 11 and 12), while the crosses joined by dotted lines show the profiles for the 2008 data set derived by Hunt et al. (2014, 2015).

Figure 18a shows the northern PPO system current profiles in the northern hemisphere (the solid line corrected profile in Figure 11b for the 2012/2013 data set). The forms of the two determinations are seen to be fairly similar, though with a reversal in the sense of the current at a larger northern colatitude for the 2012/2013 data set than for the 2008 data and with a peak at a modestly smaller value at a modestly smaller colatitude. The return region of lesser current flowing at larger colatitudes beyond the peak (see Figure 1e) also appears to be sharper in the 2012/2013 data than in 2008. Figure 18b similarly compares the southern PPO system current profiles in the northern hemisphere, which are again seen to be similar in form though again differing in detail at colatitudes around the OCB and with generally smaller values for the 2012/2013 data set than for the 2008 data.

Figure 18c shows the southern PPO system current profiles in the southern hemisphere (the solid line corrected profile in Figure 12c for the 2012/2013 data). The profiles from the two intervals are again similar, though again the return current region flowing at larger colatitudes beyond the peak appears to be sharper in the 2012/2013 data than in 2008. We do not show a comparison of the northern PPO system profile in the southern hemisphere in this case, since Hunt et al. (2014, 2015) found little evidence of northern PPO modulations in the southern hemisphere in the 2008 data.

4. Summary

In this paper we have analyzed azimuthal magnetic field data from the third interval of highly inclined orbits of the Cassini spacecraft during 2012/2013, which allow study of the nightside perturbations associated with field-aligned magnetosphere-ionosphere coupling currents. This interval occurred during Saturn northern spring when the latitude of the Sun varied between +15° and +19°. A primary comparator data set was that obtained during the second interval of highly inclined orbits in 2008, analyzed previously by Hunt et al. (2014, 2015), which similarly allows study of the nightside coupling currents but under late southern summer conditions when the latitude of the Sun varied from −8° to −4°. An important topic, therefore, has been a comparison of these pre equinox and postequinox data to identify seasonal or other differences. With regard to PPO conditions, previous work has shown that the southern system period was longer than the northern during both intervals but with a significantly larger separation during 2008 than during 2012/2013 (Andrews et al., 2012; Provan et al., 2013, 2014, 2016). Nevertheless, the 2012/2013 interval encompassed approximately four PPO beat periods, so that a full range of relative phases was experienced. A further difference is that the near-periapsis equatorial crossings during 2012/2013 were at larger radii (~6–8 R_S) than during 2008 (~3–6 R_S). Consequently, the 2012/2013 traversals were slower than during 2008 and do not approximate to snapshots of the current systems at fixed PPO phases, thus requiring statistical rather than a pass-by-pass analysis. The whole 2012/2013 data set has thus been combined into 90° × 90° "squares" of northern and southern PPO phase then used to determine colatitude profiles of the ionospheric meridional current, from which the subcorotation and PPO-related currents have been separated. Principal results are as follows.

4.1. Subcorotation Currents

In the northern (summer) hemisphere in 2012/2013 significant meridional currents are present to the smallest colatitudes observed ~8°, slowly rising from ~0.5 to ~1 MA rad^{-1} at ~15° (~1.5° equatorward of the OCB), then falling more rapidly to near-zero values at ~17.5°. Assuming axisymmetry, the total downward currents in these regions are ~3 MA in the unobserved poleward region, implying an averaged current density of ~17 nA m^{-2}, with a further ~3 MA flowing downward in the trans-OCB ring between ~8° and ~15°, with a lower current density of ~7 nA m^{-2}. The total polar downward current is thus ~6 MA, which returns up along the field in the auroral region ring between ~15° and ~17.5°, with an implied averaged current density of ~27 nA m^{-2}. The latter value, however, is no doubt strongly reduced from typical peak values in individual cases by data averaging. The upward current region maps equatorially between ~10 and ~17 R_S according to the field model employed here.

In the southern (winter) hemisphere the current has small (and unphysical negative) values from the poleward limit at ~8° to ~11° southern colatitude, rising to a 1 MA rad^{-1} peak just equatorward of the OCB at ~16°. The total downward current in this region is thus again ~6 MA, now flowing principally in a ~5° ring of open field lines bordering the OCB, with an averaged current density of ~16 nA m^{-2}. The current falls more gradually to small values on closed field lines between ~17° and ~22.5°, with an averaged upward current

density of ~10 nA m^{-2}. The upward current maps equatorially between ~6.5 and ~16 R_S, thus in to somewhat smaller radial distances than the northern upward current.

Comparison of these results with those of Hunt et al. (2014, 2015) for the 2008 data set reveals very similar polar region asymmetries but in opposite hemispheres, thus showing the effects to be seasonal. The near-zero currents at smallest colatitudes under winter conditions are taken to be due to the lack of both insolation and particle precipitation in this central open field region leading to very low ionospheric conductivities. The lack of conjugacy on closed field lines noted above, unexpected in simple theoretical models (e.g., Cowley, Bunce, & O'Rourke, 2004), was also present in opposite hemispheres in the 2008 data (Hunt et al., 2015).

4.2. PPO-Related Currents

We now summarize results concerning the northern and southern PPO current systems, discussed in terms of the maximal currents per radian of azimuth flowing on the $\Psi_{N,S} = 90° - 270°$ PPO meridians (as in Figure 15). Assuming that these currents vary near sinusoidally with PPO phase, however, and taking account of the likely small reduction in quoted peak values by a factor of ~0.9 resulting from data averaging in 90° × 90° phase squares (section 3.3), current per radian can simply be converted to total current of a given sense by multiplying by a factor of ~2.2 (section 3.7). For the northern PPO system the main field-aligned current in the northern hemisphere flows in a ~3° colatitude band whose poleward boundary lies just equatorward of the OCB and whose equatorward boundary maps to the equatorial plane at ~11 R_S, thus essentially collocated with the auroral upward currents of the subcorotation system. The magnitude of this maximum field-aligned current is ~1.2 MA rad^{-1}, flowing upward at $\Psi_N = 90°$ and downward at $\Psi_N = 270°$, with a peak current density of ~46 nA m^{-2}, such that the total field-aligned current of a given sense flowing in the northern hemisphere is ~2.7 MA, approximately half that of the upward auroral region current of the subcorotation system, which totals to ~6 MA. Where the northern PPO current flows out of the ionosphere the combined total auroral region upward current is thus approximately doubled, while where it flows into the ionosphere it is approximately canceled (Figure 11d). Similarly, for the southern PPO system the magnitude of the maximum main field-aligned current in the southern hemisphere is ~1.3 MA rad^{-1}, flowing downward at $\Psi_S = 90°$ and upward at $\Psi_S = 270°$, with a peak current density of ~23 nA m^{-2}. This current is again essentially collocated with the auroral upward current of the subcorotation system and is of comparable magnitude, flowing in a ~5° colatitude band from just equatorward of the OCB to ~20° southern colatitude mapping to ~9 R_S in the equatorial plane. For both these systems ~20% of the main field-aligned current is contributed from the polar ionosphere in the corresponding hemisphere (none from the opposite hemisphere) and ~80% from closed field lines at larger colatitudes, indicating that the principal component of these current systems consists of the adjacent field-aligned current layers of reversed sense flowing on closed field lines in a given PPO meridional sector (Figure 16). The cross-over point between the meridional currents of opposite senses contributed from the polar and closed field regions, indicative of a reversal in sense of the PPO-related ionospheric flow (Figure 1d), is located on closed field lines at ~15° colatitude in the northern hemisphere (~16.5° colatitude in the southern hemisphere), mapping equatorially to ~17 R_S. Of the main PPO field-aligned currents in both hemispheres, approximately half closes via the magnetosphere and half via the opposite hemisphere (Figure 16). With regard to overall current closure, however, we note that ~35% of the total current remains flowing in the ionosphere equatorward of the region to which these data provide access, so that the closure of this component cannot be addressed.

Comparison of the 2012/2013 PPO-related current profiles with those derived from the 2008 data shows overall similarity, though current magnitudes are generally modestly less in the 2012/2013 data set, thus reflecting similar results obtained by Provan et al. (2016) from analysis of unfiltered azimuthal field data on equatorial passes during this interval (Figure 3e). The principal difference is that the currents in both the northern and southern hemispheres appear to be similarly dual modulated in the 2012/2013 data set, with the amplitude from the opposite hemisphere being approximately half that of a given hemisphere both north and south (Figure 16), while only the northern hemisphere currents were clearly dual modulated in 2008. The return currents in the 2012/2013 data also appear to be sharper and confined to smaller colatitudes than in the 2008 data set, though the coverage of colatitude is more restricted in 2012/2013. Unlike the subcorotation currents, therefore, the differences in PPO-related currents noted here appear to be related in a more complex way to Saturn's seasons.

Appendix A: Passes in the 2012/2013 Data Set With Atypical Signatures

As indicated in section 2.1, 3 polar passes from the 2012/2013 data set, out of a total of 52, were excluded from the statistical study presented due to the presence of atypical azimuthal field and hence current signatures (as in the prior studies of the 2008 data set by Hunt et al., 2014, 2015). In this appendix we exhibit these data and briefly comment on them. The data from these passes, namely, from the northern hemisphere passes on Revs 173 and 182, and the southern hemisphere pass on Rev 169, are shown in Figures A1a and A1b, respectively, in a similar format to Figures 7b and 7d, respectively. The pale blue data in each figure reproduce the I_m meridional current profiles versus ionospheric colatitude $\theta_{iN,S}$ shown in each of the latter figures (derived using the corrected azimuthal field), serving here only to indicate the range of variability in the northern and southern hemisphere data that have been included in the study. The data from the excluded passes (again using the corrected azimuthal field) are then overplotted, in red and orange in Figure A1a for Revs 173 and 182, respectively, and red in Figure A1b for Rev 169. It can be seen that the data
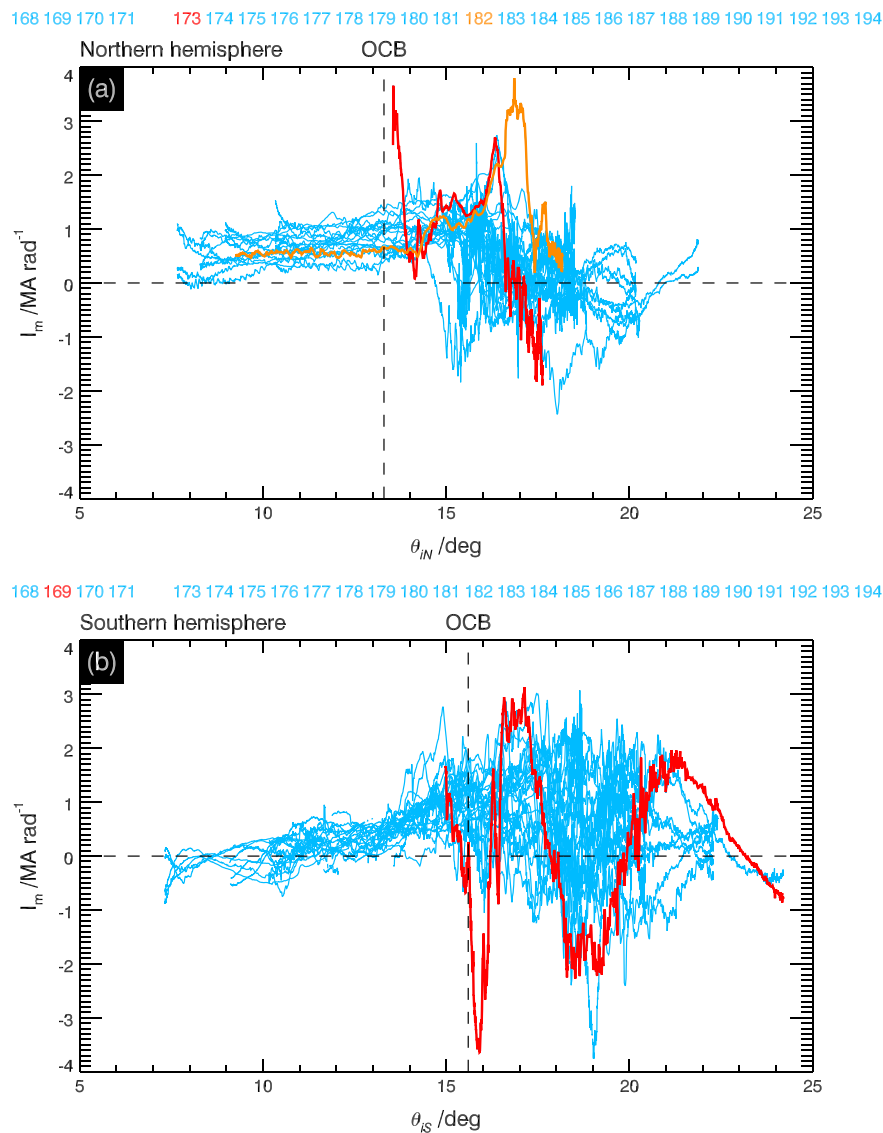
Figure A1. Plots comparing the ionospheric meridional current profiles from passes excluded from this study (red and orange) with those which have been included (pale blue) reproduced from Figures 7b and 7d. (a) The I_m profiles from the excluded northern hemisphere passes from Revs 173 (red) and 182 (orange) plotted versus northern ionospheric colatitude θ_{iN} and (b) the I_m profile from excluded southern hemisphere pass from Rev 169 (red) plotted versus southern ionospheric colatitude θ_{iS}. The vertical black dashed line shows the averaged position of the OCB in the northern hemisphere (Jinks et al., 2014).

shown in red (northern Rev 173 and southern Rev 169) both exhibit large and atypical current signatures just equatorward of the OCB in each hemisphere, which are not matched on any of the other passes. The data shown in orange (northern Rev 182) similarly exhibit a large positive current peak at ~17° whose value is around twice that of any other pass in this vicinity. These signatures are taken to be evidence of the occurrence of unusual and relatively short-lived (one ~1-day pass or less) dynamic activity taking place within the magnetosphere during these passes (e.g., Bunce et al., 2010). Due to the modest size of our overall data set, inclusion of such "outlier" data risks overly influencing analysis outcomes, particularly those obtained by division of the data into phase squares as shown in Figures 9 and 10.

References

Alexeev, I. I., Kalegaev, V. V., Belenkaya, E. S., Bobrovnikov, S. Y., Bunce, E. J., Cowley, S. W. H., & Nichols, J. D. (2006). A global magnetic model of Saturn's magnetosphere, and a comparison with Cassini SOI data. *Geophysical Research Letters*, *33*, L08101. https://doi.org/10.1029/2006GL025896

Andrews, D. J., Coates, A. J., Cowley, S. W. H., Dougherty, M. K., Lamy, L., Provan, G., & Zarka, P. (2010). Magnetospheric period oscillations at Saturn: Comparison of equatorial and high-latitude magnetic field periods with north and south SKR periods. *Journal of Geophysical Research*, *115*, A12252. https://doi.org/10.1029/2010JA015666

Andrews, D. J., Cowley, S. W. H., Dougherty, M. K., Lamy, L., Provan, G., & Southwood, D. J. (2012). Planetary period oscillations in Saturn's magnetosphere: Evolution of magnetic oscillation properties from southern summer to post-equinox. *Journal of Geophysical Research*, *117*, A04224. https://doi.org/10.1029/2011JA017444

Andrews, D. J., Cowley, S. W. H., Dougherty, M. K., & Provan, G. (2010). Magnetic field oscillations near the planetary period in Saturn's equatorial magnetosphere: Variation of amplitude and phase with radial distance and local time. *Journal of Geophysical Research*, *115*, A04212. https://doi.org/10.1029/2007JA014729

Bagenal, F., & Delamere, P. A. (2011). Flow of mass and energy in the magnetospheres of Jupiter and Saturn. *Journal of Geophysical Research*, *116*, A05209. https://doi.org/10.1029/2010JA016294

Belenkaya, E. S., Cowley, S. W. H., Badman, S. V., Blokhina, M. S., & Kalegaev, V. V. (2008). Dependence of the open-closed field line boundary in Saturn's ionosphere on both the IMF and solar wind dynamic pressure: Comparison with the UV auroral oval observed by the HST. *Annales Geophysicae*, *26*(1), 159–166. https://doi.org/10.5194/angeo-26-159-2008

Bunce, E. J., Arridge, C. S., Clarke, J. T., Coates, A. J., Cowley, S. W. H., Dougherty, M. K., et al. (2008). Origins of Saturn's aurora: Simultaneous observations by Cassini and the Hubble Space Telescope. *Journal of Geophysical Research*, *113*, A09209. https://doi.org/10.1029/2008JA013257

Bunce, E. J., Cowley, S. W. H., Alexeev, I. I., Arridge, C. S., Dougherty, M. K., Nichols, J. D., & Russell, C. T. (2007). Cassini observations of the variation of Saturn's ring current parameters with system size. *Journal of Geophysical Research*, *112*, A10202. https://doi.org/10.1029/2007JA012275

Bunce, E. J., Cowley, S. W. H., Talboys, D. L., Dougherty, M. K., Lamy, L., Kurth, W. S., et al. (2010). Extraordinary field-aligned current signatures in Saturn's high-latitude magnetosphere: Analysis of Cassini data during Revolution 89. *Journal of Geophysical Research*, *115*, A10238. https://doi.org/10.1029/2010JA015612

Bunce, E. J., Grodent, D. C., Jinks, S. L., Andrews, D. J., Badman, S. V., Coates, A. J., et al. (2014). Cassini nightside observations of the oscillatory motion of Saturn's northern auroral oval. *Journal of Geophysical Research*, *119*, 3528–3543. https://doi.org/10.1029/2013JA019527

Burton, M. E., Dougherty, M. K., & Russell, C. T. (2010). Saturn's internal planetary magnetic field. *Geophysical Research Letters*, *37*, L24105. https://doi.org/10.1029/2010GL045148

Carbary, J. F. (2012). The morphology of Saturn's ultraviolet aurora. *Journal of Geophysical Research*, *117*, A06210. https://doi.org/10.1029/2012JA017670

Carbary, J. F., & Mitchell, D. G. (2013). Periodicities in Saturn's magnetosphere. *Reviews of Geophysics*, *51*(1), 1–30. https://doi.org/10.1002/rog.20006

Cowley, S. W. H. (2000). Magnetosphere-ionosphere interactions: A tutorial review. In S. Ohtani, R. Fujii, M. Hesse, & R. L. Lysak (Eds.), *Magnetospheric current systems, Geophys. Monograph 118*, (pp. 91–106). Washington, USA: AGU Publ.

Cowley, S. H. W., Arridge, C. S., Bunce, E. J., Clarke, J. T., Coates, A. J., et al. (2008). Auroral current systems in Saturn's magnetosphere: Comparison of theoretical models with Cassini and HST observations. *Annales Geophysicae*, *26*(9), 2613–2630. https://doi.org/10.5194/angeo-26-2613-2008

Cowley, S. W. H., & Bunce, E. J. (2003). Corotation-driven magnetosphere-ionosphere coupling currents in Saturn's magnetosphere and their relation to the auroras. *Annales Geophysicae*, *21*(8), 1691–1707. https://doi.org/10.5194/angeo-21-1691-2003

Cowley, S. W. H., Bunce, E. J., & O'Rourke, J. M. (2004). A simple quantitative model of plasma flows and currents in Saturn's polar ionosphere. *Journal of Geophysical Research*, *109*, A05212. https://doi.org/10.1029/2003JA010375

Cowley, S. W. H., Bunce, E. J., & Prangé, R. (2004). Saturn's polar ionospheric flows and their relation to the main auroral oval. *Annales Geophysicae*, *22*(4), 1379–1394. https://doi.org/10.5194/angeo-22-1379-2004

Espinosa, S. A., & Dougherty, M. K. (2000). Periodic perturbations in Saturn's magnetic field. *Geophysical Research Letters*, *27*(17), 2785–2788. https://doi.org/10.1029/2000GL000048

Galand, M., Moore, L., Mueller-Wodarg, I., Mendillo, M., & Miller, S. (2011). Response of Saturn's auroral ionosphere to electron precipitation: Electron density, electron temperature, and electrical conductivity. *Journal of Geophysical Research*, *116*, A09306. https://doi.org/10.1029/2010JA016412

Gurnett, D. A., Lecacheux, A., Kurth, W. S., Persoon, A. M., Groene, J. B., Lamy, L., et al. (2009). Discovery of a north-south asymmetry in Saturn's radio rotation period. *Geophysical Research Letters*, *36*, L16102. https://doi.org/10.1029/2009GL039621

Gurnett, D. A., Persoon, A. M., Kopf, A. J., Kurth, W. S., Morooka, M. W., Wahlund, J. E., et al. (2010). A plasmapause-like density boundary at high latitudes in Saturn's magnetosphere. *Geophysical Research Letters*, *37*, L16806. https://doi.org/10.1029/2010GL044466

Hill, T. W. (1979). Inertial limit on corotation. *Journal of Geophysical Research*, *84*(A11), 6554–6558. https://doi.org/10.1029/JA084iA11p06554

Hunt, G. J., Cowley, S. W. H., & Nichols, J. D. (2018). Ionospheric currents due to ionosphere-magnetosphere coupling at Jupiter and Saturn. In A. Keiling, O. Marghitu, & M. Wheatland (Eds.), *Electric currents in geospace and beyond, Geophysical Monograph* (Vol. 235, pp. 459–475). Hoboken, NJ: John Wiley. https://doi.org/10.1002/9781119324522.ch27

Hunt, G. J., Cowley, S. W. H., Provan, G., Bunce, E. J., Alexeev, I. I., Belenkaya, E. S., et al. (2014). Field-aligned currents in Saturn's southern nightside magnetosphere: Subcorotation and planetary period oscillation components. *Journal of Geophysical Research*, *119*, 9847–9899. https://doi.org/10.1002/2014JA020506

Hunt, G. J., Cowley, S. W. H., Provan, G., Bunce, E. J., Alexeev, I. I., Belenkaya, E. S., et al. (2015). Field-aligned currents in Saturn's northern nightside magnetosphere: Evidence for interhemispheric current flow associated with planetary period oscillations. *Journal of Geophysical Research*, *120*, 7552–7584. https://doi.org/10.1002/2015JA021454

Hunt, G. J., Cowley, S. W. H., Provan, G., Bunce, E. J., Alexeev, I. I., Belenkaya, E. S., et al. (2016). Field-aligned currents in Saturn's magnetosphere: Local time dependence of southern summer currents in the dawn sector between midnight and noon. *Journal of Geophysical Research*, *121*, 7785–7804. https://doi.org/10.1002/2016JA022712

Isbell, J., Dessler, A. J., & Waite, J. H. Jr. (1984). Magnetospheric energization by interaction between planetary spin and the solar wind. *Journal of Geophysical Research*, *89*(A12), 10716–10,722. https://doi.org/10.1029/JA089iA12p10716

Jackman, C. M., & Cowley, S. W. H. (2006). A model of the plasma flow and current in Saturn's polar ionosphere under conditions of strong Dungey cycle driving. *Annales Geophysicae*, *24*(3), 1029–1055. https://doi.org/10.5194/angeo-24-1029-2006

Jia, X., & Kivelson, M. G. (2012). Driving Saturn's magnetospheric periodicities from the upper atmosphere/ionosphere: Magnetotail response to dual sources. *Journal of Geophysical Research*, *117*, A11219. https://doi.org/10.1029/2012JA018183

Jia, X., Kivelson, M. G., & Gombosi, T. I. (2012). Driving Saturn's magnetospheric periodicities from the upper atmosphere/ionosphere. *Journal of Geophysical Research*, *117*, A04215. https://doi.org/10.1029/2011JA017367

Jinks, S. L., Bunce, E. J., Cowley, S. W. H., Provan, G., Yeoman, T. K., Arridge, C. S., et al. (2014). Cassini multi-instrument assessment of Saturn's polar cap boundary. *Journal of Geophysical Research*, *119*, 8161–8177. https://doi.org/10.1029/2013JA020367

Kanani, S. J., Arridge, C. S., Jones, G. H., Fazakerley, A. N., McAndrews, H. J., Sergis, N., et al. (2010). A new form of Saturn's magnetopause using a dynamic pressure balance model, based on in situ, multi-instrument Cassini measurements. *Journal of Geophysical Research*, *115*, A06207. https://doi.org/10.1029/2009JA014262

Kellett, S., Arridge, C. S., Bunce, E. J., Coates, A. J., Cowley, S. W. H., Dougherty, M. K., et al. (2011). Saturn's ring current: Local time dependence and temporal variability. *Journal of Geophysical Research*, *116*, A05220. https://doi.org/10.1029/2010JA016216

Mardia, K. V., & Jupp, P. E. (2000). *Directional statistics*. Chichester, U.K.: Wiley.

Markwardt, C. B. (2009). Non-linear least-squares fitting in IDL with MPFIT, *Astron. Data Anal Softw. Syst. XVIII ASP Conf. Ser.*, *411*.

Persoon, A. M., Gurnett, D. A., Leisner, J. S., Kurth, W. S., Groen, J. B., & Faden, J. B. (2013). The plasma density distribution in the inner region of Saturn's magnetosphere. *Journal of Geophysical Research: Space Physics*, *118*, 2970–2974. https://doi.org/10.1002/jgra.50182

Persoon, A. M., Gurnett, D. A., Santolik, O., Kurth, W. S., Faden, J. B., Groen, J. B., et al. (2009). A diffusive equilibrium model for the plasma density in Saturn's magnetosphere. *Journal of Geophysical Research*, *114*, A04211. https://doi.org/10.1029/2008JA013912

Pilkington, N. M., Achilleos, N., Arridge, C. S., Guio, P., Masters, A., Ray, L. C., et al. (2015). Internally driven large-scale changes in the size of Saturn's magnetosphere. *Journal of Geophysical Research: Space Physics*, *120*, 7289–7306. https://doi.org/10.1002/2015JA021290

Pontius, D. H. Jr., & Hill, T. W. (2009). Plasma mass loading from the extended neutral gas torus of Enceladus as inferred from the observed plasma corotation lag. *Geophysical Research Letters*, *36*, L23103. https://doi.org/10.1029/2009GL041030

Provan, G., Cowley, S. W. H., Lamy, L., Bunce, E. J., Hunt, G. J., Zarka, P., & Dougherty, M. K. (2016). Planetary period oscillations in Saturn's magnetosphere: Coalescence and reversal of northern and southern periods in late northern spring. *Journal of Geophysical Research*, *121*, 9829–9862. https://doi.org/10.1002/2016JA023056

Provan, G., Cowley, S. W. H., Sandhu, J., Andrews, D. J., & Dougherty, M. K. (2013). Planetary period magnetic field oscillations in Saturn's magnetosphere: Post-equinox abrupt non-monotonic transitions to northern system dominance. *Journal of Geophysical Research*, *118*, 3243–3264. https://doi.org/10.1002/jgra.50186

Provan, G., Lamy, L., Cowley, S. W. H., & Dougherty, M. K. (2014). Planetary period oscillations in Saturn's magnetosphere: Comparison of magnetic oscillations and SKR modulations in the post-equinox interval. *Journal of Geophysical Research*, *119*, 7380–7401. https://doi.org/10.1002/2014JA020011

Read, P. L., Dowling, T. E., & Schubert, G. (2009). Saturn's rotation period from its atmospheric planetary-wave configuration. *Nature*, *460*(7255), 608–610. https://doi.org/10.1038/nature08194

Southwood, D. J., & Cowley, S. W. H. (2014). The origin of Saturn magnetic periodicities: Northern and southern current systems. *Journal of Geophysical Research*, *119*, 1563–1571. https://doi.org/10.1002/2013JA019632

Southwood, D. J., & Kivelson, M. G. (2009). The source of Saturn's periodic radio emission. *Journal of Geophysical Research*, *114*, A09201. https://doi.org/10.1029/2008JA013800

Talboys, D. L., Arridge, C. S., Bunce, E. J., Coates, A. J., Cowley, S. W. H., & Dougherty, M. K. (2009). Characterization of auroral current systems in Saturn's magnetosphere: High-latitude Cassini observations. *Journal of Geophysical Research*, *114*, A06220. https://doi.org/10.1029/2008JA013846

Talboys, D. L., Arridge, C. S., Bunce, E. J., Coates, A. J., Cowley, S. W. H., Dougherty, M. K., & Khurana, K. K. (2009). Signatures of field-aligned currents in Saturn's nightside magnetosphere. *Geophysical Research Letters*, *36*, L19107. https://doi.org/10.1029/2009GL039867

Talboys, D. L., Bunce, E. J., Cowley, S. W. H., Arridge, C. S., Coates, A. J., & Dougherty, M. K. (2011). Statistical characteristics of field-aligned currents in Saturn's nightside magnetosphere. *Journal of Geophysical Research*, *116*, A04213. https://doi.org/10.1029/2009JA016102